15 Correlated Electrons out of Equilibrium: Non-Equilibrium DMFT

Martin Eckstein

University of Erlangen-Nürnberg

91058 Erlangen

Contents

1   Introduction

The conventional way to manipulate materials properties involves changes of external parameters such as pressure or magnetic fields on time scales which are slow compared to the intrinsic relaxation times in the solid. The theoretical understanding of condensed matter phases can therefore largely be build on the assumption that solids are locally in thermal equilibrium at all times. This has changed with the availability of femtosecond laser pulses, which can be used to excite a system and probe its dynamics before the return to equilibrium [1]. Such experiments have opened a new field of research in condensed matter physics with many facets:

- **Time-resolved spectroscopy**: Femtosecond pulses are available in a wide frequency range, including the THz, infra-red, visible, or X-ray domain. One can therefore make both excitation and probe selective to certain degrees of freedom, and thus observe in real time how energy is passed on after an excitation. For example, electronic relaxation processes can be revealed by measuring the population dynamics in the conduction band using time-resolved photoemission spectroscopy, or one can distinguish charge-density waves of lattice or electronic origin by how fast they can be quenched [2].

- **Materials design out of equilibrium**: Other than thermal excitation, which typically results in a suppression of all ordered states, a sufficiently strong ultra-short excitation can enhance electronic orders or reveal collective phases which are not represented in the equilibrium phase diagram. This is, in particular, relevant if the equilibrium phase diagram results from competing effects. For example, signatures of light-induced superconductivity have been observed in various materials [3,4], electronic excitation can enhance the order parameter in an exciton condensate [5], and changes of the electron population can close the gap in VO_2 [6]. In a number of cases femtosecond excitation eventually results in hidden states, i.e., long-lived metastable states with new types of magnetic and orbital order, which are entirely inaccessible along thermodynamic pathways [7,8].

- **Dynamical stabilization**: Dynamical stabilization implies the modification of properties *while* a system is driven by an external perturbation. Experimentally established is the technique of nonlinear phononics [9], by which the lattice structure is deformed transiently along the coordinates of phonons which couple anharmonically to selectively excited modes. More generally, when a system with some nonlinearity, which may be the interaction or the dependence of the dispersion $\varepsilon(\boldsymbol{k})$ on $\boldsymbol{k}$, is periodically driven, its period-averaged dynamics and can be understood in terms of a so-called Floquet Hamiltonian, which can qualitatively differ from the un-driven Hamiltonian [10]. Examples include band-structure control (e.g., the generation of topologically nontrivial bands by circularly polarized light [11]), or a manipulation of low energy Hamiltonians (superconducting pairing [12,13], spin-exchange [14]). While the latter has been demonstrated in cold atoms [15], a potential application of this so-called Floquet engineering to real solids hinges on the question of heating.

- **Strong-field physics**: On the femtosecond timescale, a solid can endure external fields of the order volts per lattice constant, which would lead to an immediate breakdown of the material in the steady state. Such fields can be used to drive coherent non-equilibrium dynamics, in which electrons explore a sizeable fractions of the Brillouin zone, leading to phenomena like high-harmonic generation in solids [16].

A challenge for the investigation of non-equilibrium states in solids is that many fundamental concepts of condensed mater physics rely on thermal equilibrium. An important example is the electronic structure itself. Quasi-particles in correlated systems may become ill-defined by a non-equilibrium excitation which involves a substantial population of states far from the Fermi surface. In this limit, even a theoretical approach based on kinetic equations, which provides an intuitive rate-equation for the time-dependent population of electrons in a given ("rigid") band structure, becomes questionable. Below we will describe how real-time Green functions give an interpretation of the electronic structure in non-equilibrium states. Another fundamental question is how fast and whether an interacting system *thermalizes* after a perturbation [17]. In many cases, the energy deposited by a laser in the electronic system would imply electronic temperatures large enough to melt, rather than enhance, various orders. However, beyond a description based on a Boltzmann equation the understanding of thermalization is not obvious. In general, thermalization can be delayed by the presence of a gap. In the strongly interacting Hubbard model, thermalization after an sudden turn-on of the interaction can happen on the ultra-fast time-scale of the inverse hopping, but only in a narrow regime of interactions [18]. Ideal integrable model systems never thermalize, and even though such models hardly find an exact representation in condensed matter, the vicinity to an integrable point can result in a two-stage relaxation where the earlier stage (pre-thermalization) is governed by the integrable dynamics [19] and can feature long-range order even when the final thermal state does not.

In these notes we attempt an understanding of the many-body dynamics in solids from a model perspective. For a general discussion, let us take the Hubbard model as a paradigmatic example

$$H(t) = -\sum_{ij,\sigma} v_{ij}(t)\, c_{i\sigma}^\dagger c_{j\sigma} + U\sum_i c_{i\uparrow}^\dagger c_{i\uparrow} c_{i\downarrow}^\dagger c_{i\downarrow}. \tag{1}$$

Here, $c_{i\sigma}^\dagger$ ($c_{i\sigma}$) create (annihilate) an electron with spin σ at site i of a crystal lattice, v_{ij} is the hopping matrix element, and electrons interact via a local Coulomb interaction U. Taking this model (or its multi-orbital variants) as a faithful representation of the electronic properties, we can ask how the state of the system evolves from a given initial state, which is usually the thermal ensemble for the Hamiltonian $H(0)$. Time-dependent electromagnetic fields (the laser excitation) are most easily included by a Peierls substitution, which introduces the vector potential $\boldsymbol{A}(\boldsymbol{r},t)$ as a phase factor in the hopping matrix elements,

$$v_{ij}(t) = v_{ij}\, \exp\left(-\frac{ie}{\hbar}\int_{\boldsymbol{R}_i}^{\boldsymbol{R}_j} d\boldsymbol{r}\, \boldsymbol{A}(\boldsymbol{r},t)\right), \tag{2}$$

and adds a scalar potential term $e\sum_{i\sigma}\varPhi(\boldsymbol{R}_i,t)\,c_{i\sigma}^\dagger c_{i\sigma}$ to the Hamiltonian (e is the charge of an electron). When we are interested in the action of optical or THz fields, the wavelength is

much longer than the lattice spacing, and the field can be approximated as space-independent, with $\boldsymbol{E}(t) = -\partial_t \boldsymbol{A}(t)$ and $\Phi = 0$. Including electric fields in multi-band models is more subtle, because the Peierls substitution does not describe inter-band dipole couplings or Stark shifts of the Wannier orbitals. We also note that the Hamiltonian (1) describes only electronic motion, while in a solid also the lattice dynamics does play a role at longer times. Unless we are interested in a specific response such as a deformation of the lattice, we may account for this by including the phonons as a dissipative environment (heat bath), which is relatively straightforward in the Keldysh formalism used below. In many cases of interest, however, only short times are of interest, on which electrons may safely be considered as an isolated system.

The Keldysh formalism provides the framework to discuss many-body physics for transient and steady-state non-equilibrium situations (diagrammatic perturbation theory, path integrals). All diagrammatic approximations, such as perturbation theory, GW, etc., can be reformulated in the time-domain, by replacing imaginary-time arguments and frequencies by times on a more general real-time contour, only the numerical evaluation of the resulting equations in real-time is far more costly, as discussed below. Regarding correlated materials, dynamical mean-field theory (DMFT) [20] and its extensions present a very versatile approach to obtain the electronic structure even from first principles, as discussed in previous lectures of this series [21]. Like any other many-body formalism based on imaginary time, DMFT can be reformulated for the real-time dynamics, as noted first in [22, 23]. Although the evaluation of the DMFT equations is more challenging (in particular the solution of the auxiliary impurity problem), non-equilibrium DMFT has since then been applied to a wide range of topics [24], including the dynamics after quenches and dynamical phase transitions in various ideal model systems, the study of photo-induced dynamics in Mott insulators, the understanding of light-induced phases (manipulation of magnetic interactions, light-induced superconductivity, hidden states with spin and orbital order), the investigation of strong-field phenomena in correlated systems such as the dielectric breakdown and high-harmonic generation, and the properties of periodically driven states (Floquet engineering).

In these notes we explain the foundations of non-equilibrium DMFT in the Keldysh formalism, and then discuss the photo-induced dynamics in Mott insulators to illustrate the approach.

2   The Keldysh formalism

This section presents a brief summary on the Keldysh formalism. For an in-depth introduction we refer to standard textbooks, e.g., [25, 26].

2.1   Two-time Green functions and electronic structure

The Keldysh formalism is based on Green functions $G(i, t, j, t')$, that describe the propagation of particles and holes between orbitals i, j and times t, t'. It is convenient to start from the

following electron and hole propagators, as introduced by Kadanoff and Baym,

$$G_{\boldsymbol{k}}^<(t, t') = +i\langle c_{\boldsymbol{k}}^\dagger(t') c_{\boldsymbol{k}}(t)\rangle \tag{3}$$

$$G_{\boldsymbol{k}}^>(t, t') = -i\langle c_{\boldsymbol{k}}(t) c_{\boldsymbol{k}}^\dagger(t')\rangle. \tag{4}$$

Here $c_{\boldsymbol{k}}^\dagger$ and $c_{\boldsymbol{k}}$ denote creation and annihilation operators for an electron in a single-particle orbital $\boldsymbol{k}$. (Only momentum $\boldsymbol{k}$ is shown for simplicity of notation, but spin or orbital indices may easily be added.) The time-dependence of the operators is understood in the Heisenberg picture, and $\langle \cdots \rangle = \mathrm{Tr}(\rho_0 \cdots)/Z$ is an average using the density matrix of the initial state. These Green functions describe the propagation of an additional electron or hole on top of the many-body state, and therefore contain the full information on all single-particle observables. In the following we discuss their properties in equilibrium states, so-called non-equilibrium steady states, and a general time-evolving state:

- **Equilibrium:** In equilibrium, translational invariance in time implies that the propagators (3) and (4) depend only on the time-difference, and one can introduce the Fourier transform $G(\omega) = \int dt\, e^{i\omega t} G(t, 0)$. A straightforward expansion of the Green functions in (many-body) energy eigenstates leads to the relations

$$G_{\boldsymbol{k}}^<(\omega) = \quad 2\pi i A_{\boldsymbol{k}}(\omega)\, f(\omega) \qquad \equiv \quad 2\pi i N_{\boldsymbol{k}}^<(\omega), \tag{5}$$

$$G_{\boldsymbol{k}}^>(\omega) = -2\pi i A_{\boldsymbol{k}}(\omega)[1 - f(\omega)] \equiv -2\pi i N_{\boldsymbol{k}}^>(\omega). \tag{6}$$

  Here we have introduced the (many-body) spectral function $A_{\boldsymbol{k}}(\omega)$, which is defined in terms of the retarded Green function as

$$A_{\boldsymbol{k}}(\omega) = -\frac{1}{\pi} \mathrm{Im} \int dt\, e^{i(\omega+i0)t} G_{\boldsymbol{k}}^R(t), \tag{7}$$

$$G_{\boldsymbol{k}}^R(t - t') = \theta(t - t') \left(G_{\boldsymbol{k}}^>(t - t') - G_{\boldsymbol{k}}^<(t - t') \right). \tag{8}$$

  The equations show that equilibrium states are characterized by the spectral function only, which contains information about the band structure, including the position of the bands, and the lifetime of quasiparticles. The occupation (which is, e.g., measured in photo-emission) is linked to the spectrum by a *universal occupation function* $f(\omega)$ which only depends on temperature.

- **Non-equilibrium steady states:** An important application of the Keldysh formalism is to study non-equilibrium steady states. When the system is simultaneously subject to a time-independent perturbation and coupled to external reservoirs (e.g., metallic leads with a voltage bias), we can assume that any transients after the initial switch-on of the perturbation decay with time, until energy (particle) absorption from the perturbation is balanced by dissipation into the bath. The system then resides in a steady state in which all correlation functions are translationally invariant in time, but yet the system is not in a thermal equilibrium state: We have $G_{\boldsymbol{k}}^<(\omega) = 2\pi i A_{\boldsymbol{k}}(\omega) F_{\boldsymbol{k}}(\omega)$ and $G_{\boldsymbol{k}}^>(\omega) = -2\pi i A_{\boldsymbol{k}}(\omega)(1 - F_{\boldsymbol{k}}(\omega))$ like in Eqs. (5) and (6) with a positive definite spectral function $A_{\boldsymbol{k}}(\omega)$ and occupation function $F_{\boldsymbol{k}}(\omega)$, but $F_{\boldsymbol{k}}$ is not given by the Fermi function.

- **Transient time-evolution:** In a time-evolving state, time-translational invariance is lost, so that both spectral and occupation functions depend on two time-arguments separately. It is still often convenient to introduce a partial frequency dependence: A symmetric choice is the *Wigner transform* for a function $X(t, t')$, with an average time $t_{av} = (t + t')/2$ and a relative time $t_{rel} = t - t'$, and a Fourier transform with respect to t_{rel},

$$X(t_{av}, \omega) = \int dt_{rel} \; e^{i\omega t_{rel}} \; F\big(t_{av} + t_{rel}/2, t_{av} - t_{rel}/2\big). \tag{9}$$

One may introduce Wigner transforms $G^{<,>}(t, \omega)$, or equivalently time-dependent occupation functions and spectral functions. In fact, a quantum Boltzmann equation [26] is an equation of motion for a time-dependent occupation function, often supplemented with the approximation that the spectrum takes a given form. However, in a situation where both the spectrum and the occupation change at the same pace, as can easily be the case for the ultra-fast dynamics in strongly correlated condensed matter systems, the separation of spectrum and occupation becomes somewhat arbitrary. An exception is the dynamics governed by non-interacting or mean-field Hamiltonians, where in the absence of external fields the spectrum is given by the eigenvalues of a single-particle Hamiltonian, and the occupation by the corresponding expectation values of the one-particle density matrix.

Probabilistic interpretation of real-time Green functions

We can illustrate the meaning of the propagators $G^{\gtrless}$ by their relation to a time-resolved electron removal and addition experiment, such as photoemission spectroscopy. In a time- and angle-resolved photoemission experiment, one measures the probability that an electron is emitted under the action of a short probe pulse, as a function of the photo-electron energy E and the photo-electron momentum $\mathbf{k}_e$. An idealized description is obtained by adding a term $S(t - t_p) \, e^{i\Omega(t - t_p)} f^\dagger c_{\mathbf{k}} + h.c.$ to the Hamiltonian which allows a transition to an outgoing state f. The signal is the change of $\langle f^\dagger f \rangle$ during a pulse. Here Ω is the photon energy, and $S(t - t_p)$ is the time profile of the probe pulse, which is centered around a given time t_p. With respect to real photo-emission, this formulation makes three approximations: (i) the sudden approximation, which assumes that there is no interaction between the electrons in the solid and in the outgoing state f, (ii) a classical approximation of the light pulse, and (iii) a simplistic treatment of the transition matrix elements. These approximations are, however, the same as those usually made to get a rough interpretation of photo-emission results in equilibrium in terms of the occupied spectrum $A_{\mathbf{k}}(\omega) f(\omega)$. The signal can be obtained using time-dependent perturbation theory in the light-matter coupling [27], leading to (to leading order in S)

$$I_{\mathbf{k}}(E, t_p) = \int dt \, dt' \, e^{iE(t - t')}(-i) \, G^<_{\mathbf{k}}(t_p + t, t_p + t') \, S(t) \, S(t')^*. \tag{10}$$

To further illustrate Eq. (10), one can consider a Gaussian probe profile $S(t) = \exp(-t^2/2\Delta t^2)$ with duration Δt, and transform Eq. (10) to a mixed time-frequency representation

$$I_{\boldsymbol{k}}(E, t_p) \propto \int d\omega \, dt \, N^<(t_p + t, E + \omega) \, e^{-\frac{t^2}{\Delta t^2}} e^{-\omega^2 \Delta t^2}. \tag{11}$$

Here $N_{\boldsymbol{k}}^<(t,\omega) = G_{\boldsymbol{k}}^<(t,\omega)/(2\pi i)$ is related to the Wigner transform (9) of the Green function, in analogy to Eq. (5). In equilibrium we have $N_{\boldsymbol{k}}^<(\omega) = A_{\boldsymbol{k}}(\omega)f(\omega)$, so that long pulses imply the usual interpretation of the photoemission spectrum in terms of the occupied density of states, while Eq. (11) shows that in a transient state $N_{\boldsymbol{k}}^<(t,\omega)$ gives the probability distribution to remove a particle with energy $\hbar\omega$ and momentum $\boldsymbol{k}$ from the system *at time* t after averaging over a filter $e^{-\frac{t^2}{\Delta t^2}} e^{-\omega^2 \Delta t^2}$ which satisfies the energy-time uncertainty $\Delta t \, \Delta \omega = 1$ [28,29].

Fluctuation-dissipation theorem

Equations (5) and (6) provide a fermionic variant of the fluctuation-dissipation theorem, which holds more generally for any observable. The *response* of an observable X to an external force is given by the Kubo formula $\chi(t-t') = -i\theta(t-t')\langle [X(t), X(t')] \rangle$, while $C^>(t-t') = -i\langle X(t)X(t') \rangle$ correspond to the fluctuations. Again, in equilibrium all correlation functions depend on time-difference only, and an eigenstate representation yields

$$C^<(\omega) = 2ib(\omega) \, \mathrm{Im} \, \chi(\omega + i0), \tag{12}$$

where $b(\omega) = 1/(e^{\beta\omega} - 1)$ is the Bose function. This is the fluctuation-dissipation theorem, which states that the imaginary part of the response function, which describes energy dissipation, is related to the power spectrum of the fluctuations. If X is a collective excitation, such as the displacement field of phonons, $\mathrm{Im} \, \chi(\omega)$ and $C^<(\omega)$ correspond to the spectrum and the occupation of the collective mode, respectively.

The fluctuation-dissipation theorem provides a measurement to decide whether a system is in thermal equilibrium, and to determine the effective temperature of a given subset of degrees of freedom. For example, optical spectroscopy measures the polarization response to long-wavelength electric fields. A full characterization of the non-equilibrium state would require also a measurement of the noise power spectral density of the polarization (or the current). Measuring noise is generally harder than measuring the response, but recent experiments in this direction have extracted current fluctuations from the shot-to-shot variance in the measured intensity of the reflected probe-pulse in a pump-probe experiment [30].

2.2   The Keldysh contour

For an isolated system with Hamiltonian $H(t)$, the solution of the Schrödinger equation $i\partial_t |\psi(t)\rangle = H(t) |\psi(t)\rangle$ with initial condition $|\psi(t_0)\rangle = |\psi_0\rangle$ can be written in terms of the unitary time-evolution operator $\mathcal{U}(t, t_0)$

$$|\psi(t)\rangle = \mathcal{U}(t, t_0) |\psi_0\rangle, \tag{13}$$

which is defined by the differential equation $i\partial_t \mathcal{U}(t,t_0) = H(t)\mathcal{U}(t,t_0)$ with initial condition $\mathcal{U}(t_0,t_0) = 1$. Formally, the evolution operator can be written as the time-ordered product,

$$\mathcal{U}(t,t') = T_t \, e^{-i\int_{t'}^t d\bar{t}\, H(\bar{t})} \quad (\text{for } t > t'), \tag{14}$$

where the *time-ordering operator* T_t brings operators at later time to the left. The adjoint of (15) is the inverse (backward) time-evolution $\mathcal{U}(t,t')^\dagger = T_{\bar{t}} \, e^{+i\int_{t'}^t d\bar{t}\, H(\bar{t})}$, where $T_{\bar{t}}$ is the anti time-ordering operator. The time-ordered exponential can be read as the step-wise time-evolution

$$\mathcal{U}(t,t') \approx e^{-i\delta t H(t-\delta t)} \cdots e^{-i\delta t H(t'+2\delta t)} e^{-i\delta t H(t'+\delta t)} e^{-i\delta t H(t')} \quad (\text{for } t > t'), \tag{15}$$

taking the Hamiltonian constant along each infinitesimal interval, $\mathcal{U}(t+\delta t, t) = e^{-i\delta t H(t)} + \mathcal{O}(\delta t^2)$. In order to describe the time-evolution of a quantum system, we aim to compute observables or correlation functions of the general form

$$\langle \hat{O}(t) \rangle = \mathrm{Tr}\left(\rho_0 \, \mathcal{U}(t,t_0)^\dagger \hat{O} \mathcal{U}(t,t_0) \right). \tag{16}$$

Here ρ_0 is the density matrix which defines the state of the system at initial time t_0. The density matrix ρ_0 provides only the statistical weights of the initial states, while Eq. (16) describes the evolution of an isolated quantum system: If $\rho_0 = \sum_n w_n |\psi_n\rangle\langle\psi_n|$ is the statistical mixture of states $|\psi_n\rangle$, Eq. (16) can be written as

$$\langle \hat{O}(t) \rangle = \sum_n w_n \langle \psi_n(t) | \hat{O} | \psi_n(t) \rangle, \tag{17}$$

where $|\psi_n(t)\rangle = \mathcal{U}(t,t_0)|\psi_n\rangle$ is obtained by solving the unitary Schrödinger equation with initial condition $|\psi_n(t_0)\rangle = |\psi_n\rangle$. In the following, we take ρ_0 to be the Gibbs ensemble with respect to some initial Hamiltonian $H(0)$.

The time-ordering in $\mathcal{U}(t,t_0)$ and the anti-time-ordering in $\mathcal{U}(t,t_0)^\dagger$ in Eq. (16) can be combined into a single time-ordering along a time contour. The latter extends from t_0 in forward direction and then in backward direction (from now on, we will take $t_0 = 0$ without loss of generality). Moreover, the thermal density matrix can be written as a time-evolution operator along an imaginary time axis $[0, -i\beta]$, so that the three branches can be combined into a single *L-shaped contour* $\mathcal{C}$, as depicted in Fig. 1. The order of times is indicated by the arrows in the figure (from earlier to later). We will use the notation $t >_\mathcal{C} t'$ ($t <_\mathcal{C} t'$) to denote that t is later (earlier) on $\mathcal{C}$ than t'. Throughout these notes, we will denote a time argument on the upper (lower) branch by $t_\pm$ with $t \in \mathbb{R}$, respectively, and a time-argument on the vertical branch by $-i\tau$ with $\tau \in [0, \beta]$. Together with the time-contour we introduce the contour-ordering operator

$$T_\mathcal{C} A(t) B(t') = \begin{cases} A(t)B(t') & t >_\mathcal{C} t' \\ \xi B(t')A(t) & t' >_\mathcal{C} t \end{cases}. \tag{18}$$

The sign ξ is -1 if the permutation of A and B involves an odd number of permutations of fermion creation of annihilation operators, and $+1$ otherwise. With this the expectation value (16) is written as

$$\langle \hat{O}(t) \rangle = \frac{1}{Z} \mathrm{Tr}\left(T_\mathcal{C} \, e^{-i\int_\mathcal{C} d\bar{t}\, H(\bar{t})} \hat{O}(t_+) \right), \quad Z = \mathrm{Tr}\left(T_\mathcal{C} \, e^{-i\int_\mathcal{C} d\bar{t}\, H(\bar{t})} \right), \tag{19}$$
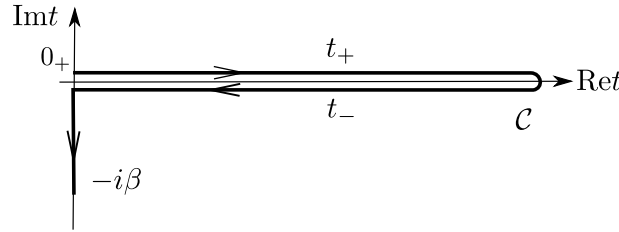
Fig. 1: *The Keldysh contour $\mathcal{C}$, ranging from time 0 to a maximum time t_{max}, back to time 0, and finally to $-i\beta$ on the imaginary-time branch. Times on the upper and lower real-time branch are denoted by t_+ and t_-, respectively. Both t_+ and t_- are real, and the index $\pm$ serves only to distinguish backward and forward time-evolution. The arrows denote the time-ordering along $\mathcal{C}$ from "earlier" to "later" contour times.*

where we have introduced integrals along the time-integrals

$$\int_{\mathcal{C}} dt\, f(t) = \int_0^{t_{\max}} dt\, f(t_+) - \int_0^{t_{\max}} dt\, f(t_-) - i \int_0^{\beta} d\tau\, f(-i\tau). \qquad (20)$$

The electron and hole propagators (3) and (4) appear now naturally as different components of a **contour-ordered Green function**

$$G_{jj'}(t,t') = -i\langle T_{\mathcal{C}}\, c_j(t) c_{j'}^{\dagger}(t')\rangle. \qquad (21)$$

By choosing the time-arguments on the upper and lower branch of the contour, respectively, we recover the lesser and greater Green functions (3) and (4) for $t, t' > 0$

$$G^{<}(t,t') = G(t_+, t'_-) \quad \text{and} \quad G^{>}(t,t') = G(t_-, t'_+). \qquad (22)$$

In turn, one can see that $G^{<}$ and $G^{>}$ suffice to restore the full Green function $G(t,t')$ on the real-time branches, so that $G(t,t')$ is equivalent to specifying the single-particle properties at all times. Without proof, we note that the mixed components $G(\tau, t)$ are one-to-one related to the correlations $G(t,t')$ with one or two arguments before $t = 0$, assuming the system is then in equilibrium.

Functional integrals and many-body theory

The introduction of the contour allows to repeat one-to-one all steps which lead to the definition of path integrals and perturbation theory in the Matsubara formalism. We can obtain the path integral for the partition function (or rather, any generating function for contour-ordered expectation values) as

$$Z = \text{Tr}\left(T_{\mathcal{C}}\, e^{-i\int_{\mathcal{C}} dt\, H(t)}\right) = \int \mathcal{D}[\bar{c}, c]\, e^{iS} \qquad (23)$$

$$S = \int_{\mathcal{C}} dt \left(\sum_j \bar{c}_j(t) i\partial_t c_j(t) - H[\bar{c}, c] \right). \qquad (24)$$

This expression is understood in the usual way as a continuum limit of a discretized time contour with timesteps t_a, $a = 0, ..., M$ along the contour ($t_0 = 0^+$ and $t_M = -i\beta$). Anti-periodic or periodic boundary conditions $c(t_0) = -c(t_M)$ are implied for bosons and fermions, respectively, and j labels all orbital degrees of freedom. Note that ∂_t is the usual time-derivative, not a derivative along the contour direction.

With the general expectation value

$$\langle \cdots \rangle_S = Z^{-1} \int \mathcal{D}[\bar{c}, c] \, e^{iS} \cdots , \tag{25}$$

we naturally arrive at the Green function

$$G_{jj'}(t, t') = -i\langle c_j(t)\bar{c}_{j'}(t')\rangle_S. \tag{26}$$

For the action (24), the latter equals the contour-ordered Greens function (21). The (anti)-periodic boundary condition of c and $\bar{c}$ imply an (anti)-periodic boundary condition for G,

$$G(0_+, t) = \pm G(-i\beta, t), \quad G(t, 0_+) = \pm G(t, -i\beta), \tag{27}$$

where the upper (lower) sign refers to the case where c and $c^\dagger$ are Bose (Fermi) operators.

Equations of motion

The action of the noninteracting problem $H(t) = \varepsilon(t) \, c^\dagger c$, $S = \int dt dt' \, \bar{c}(t) \, \delta_\mathcal{C}(t, t')(i\partial_t - \varepsilon)c(t')$ is a quadratic form, where $\delta_\mathcal{C}(t, t')$ is the delta-function consistent with the contour integral (20). The integrals $\int_\mathcal{C}$ are to be understood as the continuum limit of a discrete form $S = \sum_{a,a'} \bar{c}_a A_{aa'} c_{a'}$ where a, a' label all orbital and discrete time indices. Gaussian integration for the discrete action yields $\sum_b A_{ab} G_{ba'} = \delta_{aa'}$, i.e., $G_{aa'} = -i\langle c_a \bar{c}_{a'}\rangle_S$ and A are inverse matrices in time. Reinstating the continuum limit, the equation $A \, G = 1$ yields the equation of motion for G,

$$\int_\mathcal{C} d\bar{t} \, \delta_\mathcal{C}(t, \bar{t})(i\partial_{\bar{t}} - \varepsilon) \, G(\bar{t}, t') = \big(i\partial_t - \varepsilon(t)\big) \, G(t, t') = \delta_\mathcal{C}(t, t'). \tag{28}$$

The "derivation" of this equation has seemingly been a bit too careless, as in contrast to the inverse of the discrete matrix A, the differential equation (28) does not have a unique solution unless either an initial or boundary condition is specified. However, with the boundary condition (27) the solution is unique. For the equilibrium Green function and the single orbital Hamiltonian $H = \varepsilon \, c^\dagger c$, it is instructive to check that the solution is given by

$$G(t, t') = e^{-i\varepsilon(t-t')}\Big(if(\varepsilon) \, \theta_\mathcal{C}(t', t) - if(-\varepsilon) \, \theta_\mathcal{C}(t, t')\Big), \tag{29}$$

where $\theta_\mathcal{C}(t, t') = 1$ for $t >_\mathcal{C} t'$ and 0 otherwise. The same result is obtained from Eq. (21) and the Heisenberg equation of motion for $c(t)$ and $c^\dagger(t)$.

From now on we use a continuum notation assuming that all operations take place within the space of (anti)-periodic functions. Multiplication of two contour functions corresponds to convolution along $\mathcal{C}$

$$[A * B](t, t') = \int_\mathcal{C} d\bar{t} \, A(t, \bar{t})B(\bar{t}, t'), \tag{30}$$

$$\Sigma_{j,j}(t,t') = \quad \text{[diagram]} \quad + \quad \text{[diagram]} \quad + \quad \text{[diagram]} \quad + \cdots$$

$$j',t' \longrightarrow j,t = (G_0)_{j,j'}(t,t') \qquad \text{[diagram]} = U(t)$$

Fig. 2: *Diagrammatic representation of the local self-energy in the Hubbard model: The noninteracting Green function $G_{0,jj'}(t,t')$ is represented by a directed line, and the interaction $U(t)$ is denoted by a dashed line. The first two diagrams are $\Sigma_\sigma^{(2)}(t,t')$ and $\Sigma_\sigma^{(1)}(t,t')$, the third diagram is a non-skeleton diagram, with a self-energy insertion in one of the G_0-lines.*

and the inverse $A^{-1}(t,t')$ of a function $A(t,t')$ is understood as the differential or integral equation $\int_\mathcal{C} d\bar{t}\, A^{-1}(t,\bar{t}) A(\bar{t},t') = \int_\mathcal{C} d\bar{t}\, A(t,\bar{t}) A^{-1}(\bar{t},t') = \delta_\mathcal{C}(t,t')$ with the boundary condition (27) (additional matrix multiplication in orbital indices implied).

Diagrammatic perturbation theory

The construction of diagrammatic perturbation theory does not depend on the time contour, and is formally identical for Matsubara Green functions and contour-ordered Green functions. In particular, perturbation theory is based on the Wick theorem, which states that n-particle contour-ordered expectation values for a *quadratic action* can be factorized into a determinant of two-point correlation functions (for fermions), $\langle c_1 \cdots c_n c_{n'}^\dagger \cdots c_{1'}^\dagger \rangle_{S_0} = \det(M)$, $M_{ij'} = \langle c_i c_{j'}^\dagger \rangle_{S_0}$, (for bosons one would obtain a permanent). Wick's theorem in fact follows as a simple property of Gaussian path integrals.

We can introduce the self-energy $\Sigma(t,t')$, which is a function of two times on the contour. It can be expanded in a power series of the Green function, where each term is represented as a Feynman diagram. The topology of the diagrams is the same as in the equilibrium Matsubara formalism, only internal time-integrals in the interpretation of diagrams must be taken over the contour $\mathcal{C}$ instead of over imaginary time. The relation of non-interacting Green function and the self-energy is therefore given by the Dyson equation

$$G = G_0 + G_0 * \Sigma * G = G_0 + G * \Sigma * G_0 \tag{31}$$

$$\Leftrightarrow \quad G^{-1}(t,t') = G_0^{-1}(t,t') - \Sigma(t,t'). \tag{32}$$

For illustration and later reference, we state the explicit expression of the first and second-order diagram for the self-energy of the Hubbard model, as shown in Fig. 2,

$$\Sigma_\sigma^{(1)}(t,t') = U(t)\, n_{\bar\sigma}(t)\, \delta_\mathcal{C}(t,t'), \tag{33}$$

$$\Sigma_\sigma^{(2)}(t,t') = U(t)\, U(t')\, G_{0\sigma}(t,t')\, G_{0\bar\sigma}(t',t)\, G_{0\bar\sigma}(t,t'). \tag{34}$$

Self-consistent expansions

The sum of all Feynman diagrams generates $\Sigma[G_0]$ as a functional of G_0. One can re-sum this expansion by removing all terms in which the G_0-lines itself have self-energy insertions (such as the third diagram in Fig. 2), and in turn replace all Green function lines by the full interacting self-energy G. This results in the so-called skeleton functional $\Sigma[G]$. In combination with the Dyson equation Eq. (32), an approximation to the skeleton functional, e.g., the truncation to given order, yields a closed-form non-linear integral-differential equation for G. Although the skeleton expansion to given order generates an infinite subset of the diagrams of the bare expansion $\Sigma[G_0]$, this does not always lead to quantitatively better results. An example is the second order perturbation theory for the impurity problem in DMFT [20], where only the bare expansion can qualitatively recover the Mott transition. However, any truncation of the self-consistent skeleton expansion $\Sigma[G]$ satisfies conservation laws for energy and particle number, while an approximation to $\Sigma[G_0]$ does not [31], which is of great importance for the description of non-equilibrium dynamics. If energy is not conserved, the concept of thermalization becomes meaningless, as only the conservation laws fix the statistical properties of a system in thermal equilibrium.

2.3   Kadanoff-Baym equations

In this subsection we discuss the numerical solution of the Dyson equation in real time. We consider the standard form, obtained from (32) and the inverse $G_0^{-1} = \delta_{\mathcal{C}}(t, t')\big(i\partial_t - h(t)\big)$ (orbital indices can be added easily)

$$\big(i\partial_t - h(t)\big)G(t, t') - \int_{\mathcal{C}} d\bar{t}\, \Sigma(t, \bar{t})\, G(\bar{t}, t') = \delta_{\mathcal{C}}(t, t')\,. \tag{35}$$

This equation is a non-Markovian equation of motion for the Green function, where the self-energy takes the role of a memory kernel. To solve the equation one can take an equidistant time grid, with M time slices along $\mathcal{C}$. The operator $\big(i\partial_t - h(t)\big)\delta_{\mathcal{C}}(t, t') - \Sigma(t, t')$ can then be written as a M-dimensional matrix, and the solution for G becomes a matrix inversion. This scheme, however, does not exploit the possibility to transform Eq. (35) into a step-wise time propagation scheme: Because of the causal nature of the time-evolution, if the solution of Eq. (35) is known for real times $t, t' \le n\Delta t$, it can be extended to the domain $t, t' \le (n+1)\Delta t$ without modification of the previous times, even when Σ depends on G in a non-linear way, e.g., in the form of a perturbative expression $\Sigma[G]$. (In general, any functional expression $\Sigma[G]$ should be causal, such that $\Sigma(t, t')$ in the domain $t, t' \le n\Delta t$ can be determined from G in the same domain $t, t' \le n\Delta t$.)

On can introduce a parametrization of contour functions which allows to make use of this causality. The values of the contour-ordered function $G(t, t')$ with t and t' on different branches of $\mathcal{C}$ are not all independent, because the largest real-time argument can be shifted between the

upper to the lower contour branch. For example, for $t' < t$

$$G(t_+, t'_+) = \frac{1}{Z} \text{Tr} \left(e^{-\beta H(0)} \underbrace{\mathcal{U}(0,t)\,\mathcal{U}(t,t_{\max})}_{\mathcal{C}_-} \underbrace{\mathcal{U}(t_{\max},t)c\,\mathcal{U}(t,t')c^\dagger}_{\mathcal{C}_+}\mathcal{U}(t',0) \right) = G(t_-, t'_+).$$

(36)

The brackets indicate the part of the contour-ordered operator $T_\mathcal{C} e^{-i \int_\mathcal{C} dt H(t)}$ along the upper and lower branch, respectively. Because the time-evolution between t and $t_{\max}$ along the upper and lower branch cancel, c can be shifted between the two branches. The redundancy which follows from Eq. (36) can be resolved in an elegant way, using the so-called Keldysh rotation. Let us first focus only on the real-time branches of $\mathcal{C}$: With the two branches, one can start from a parametrization of G in terms of a 2×2 matrix

$$\hat{G}(t,t') \equiv \begin{pmatrix} G(t_+, t'_+) & G(t_+, t'_-) \\ G(t_-, t'_+) & G(t_-, t'_-) \end{pmatrix}, \quad t, t' \in \mathbb{R}.$$

(37)

The over-completeness of this representation can be removed by an invertible map (with $\hat{\tau}_3 = \text{diag}(1,-1)$)

$$\underline{G}(t,t') \equiv \hat{L}\,\hat{\tau}_3\,\hat{G}(t,t')\,\hat{L}^\dagger, \quad \text{where } \hat{L} = \frac{1}{\sqrt{2}}\begin{pmatrix} +1 & -1 \\ +1 & +1 \end{pmatrix}.$$

(38)

From the rotation we get ($G_{ab} = G(t_a, t'_b)$ for $a, b = \pm$)

$$\begin{aligned}
\underline{G}(t,t') &= \frac{1}{2}\begin{pmatrix} (G_{++} - G_{+-} + G_{-+} - G_{--}) & (G_{++} + G_{+-} + G_{-+} + G_{--}) \\ (G_{++} - G_{+-} - G_{-+} + G_{--}) & (G_{++} + G_{+-} - G_{-+} - G_{--}) \end{pmatrix} \\
&= \begin{pmatrix} G^R(t,t') & G^K(t,t') \\ 0 & G^A(t,t') \end{pmatrix}.
\end{aligned}$$

(39)

The second equality follows from the causality (36). For example, in the $(1,0)$-component we can shift the first time argument between the upper and lower contour for $t > t'$, which gives $\frac{1}{2}(G_{-+} - G_{--} - G_{-+} + G_{--}) = 0$, while for $t < t'$ we can shift the second argument, which gives $\frac{1}{2}(G_{++} - G_{++} - G_{--} + G_{--}) = 0$. In combination, $\frac{1}{2}(G_{++} - G_{+-} - G_{-+} + G_{--}) = 0$. The other components follow analogously, using the conventional definition of the retarded, advanced, and Keldysh Green functions

$$G^R(t,t') = \theta(t-t')\left(G^>(t,t') - G^<(t,t')\right),$$

(40)

$$G^A(t,t') = \theta(t'-t)\left(G^<(t,t') - G^>(t,t')\right),$$

(41)

$$G^K(t,t') = G^>(t,t') + G^<(t,t').$$

(42)

Using the Keldysh matrices, convolutions greatly simplify: restricted to the real-time branches of $\mathcal{C}$, the convolution of two contour functions $A(t,t')$ and $B(t,t')$ is given by $C(t_\alpha, t'_{\alpha'}) = \int d\bar{t}\left(A(t_\alpha, \bar{t}_+)\,B(\bar{t}_+, t'_{\alpha'}) - A(t_\alpha, \bar{t}_-)\,B(\bar{t}_-, t'_{\alpha'})\right)$, which can be written in the form

$$\hat{C}(t,t') = \int d\bar{t}\,\hat{A}(t,\bar{t})\,\hat{\tau}_3\,\hat{B}(\bar{t},t').$$

(43)

After the Keldysh rotation this becomes

$$\underline{C}(t,t') \equiv \hat{L}\,\hat{\tau}_3\,\hat{C}(t,t')\,\hat{L}^\dagger = \int d\bar{t}\,\hat{L}\,\hat{\tau}_3\,\hat{A}(t,\bar{t})\,\hat{L}^\dagger\hat{L}\,\hat{\tau}_3\,\hat{B}(\bar{t},t')\,\hat{L}^\dagger = \int d\bar{t}\,\underline{A}(t,\bar{t})\,\underline{B}(\bar{t},t'), \quad (44)$$

i.e., a simple convolution in real-time with an additional 2×2 matrix structure.

Noting that in the 2×2 matrix the derivative and delta function are $i\partial_t \hat{1}$ and $\delta(t-t')\,\hat{\tau}_3$, the Dyson equation becomes, after Keldysh rotation

$$\big(i\partial_t - h(t)\big)\underline{G}(t,t') - \int d\bar{t}\,\underline{\Sigma}(t,\bar{t})\,\underline{G}(\bar{t},t') = \delta(t,t'). \qquad (45)$$

Comparing matrix elements on both sides we have equations for the individual components of G. For illustration, let us take the $(0,0)$-component

$$\big(i\partial_t - h(t)\big)G^R(t,t') - \int_{t'}^{t} d\bar{t}\,\Sigma^R(t,\bar{t})\,G^R(\bar{t},t') = \delta(t-t'), \qquad (46)$$

which must be solved with the initial condition $G^R(t,t') = 0$ for $t < t'$. In these equations we have already taken into account that retarded components vanish for $t < t'$, and have restricted the time-arguments accordingly. This has an important consequence: In order to determine $G^R(t,t')$ in the domain $t,t' \le t_{max}$, also G and Σ have to be known only for $t,t' \le t_{max}$. Thus one can solve this equation in a time-stepping manner: With the parametrization $y(s) = G^R(t'+s,t')$, Eq. (46) can be written as a Volterra integral-differential equation of the second kind,

$$\frac{d}{ds}y(s) = q(s) + p(s)y(s) + \int_0^s d\bar{s}\,k(s,\bar{s})y(\bar{s}), \qquad (47)$$

taking $q(s) = 0$, $p(s) = -ih(s)$, $k(s,\bar{s}) = -i\Sigma^R(t'+s,t'+\bar{s})$. On an equidistant grid $s \in \{m\Delta t\}$, using a notation $y_m = y(m\Delta t)$ etc., with a trapezoidal rule for the integral and a finite difference formula for the differential term, we obtain

$$\frac{y_{n+1} - y_n}{\Delta t} = q_{n+1} + p_{n+1}y_{n+1} + \Delta t\Big(\tfrac{1}{2}y_{n+1} + \sum_{m=1}^{n} k_{n,m}\,y_m + \tfrac{1}{2}y_0\Big). \qquad (48)$$

Starting from an initial value y_0 (here, $y(0) = G^R(t',t') = -i$), this equation provides an equation of y_{n+1} in terms of y_m for $m \le n$, which can be successively applied for $n = 1,2,3,...$ to determine the full function y (see Fig. 3). In practice, accurate higher order approximations should be used for derivative and integral [32], but the basic strategy of solving the Volterra equation remains the same.

The arguments above can be extended to a causal time-propagation scheme for G on the full L-shaped contour. For completeness, we state the parametrization used in the following [33]
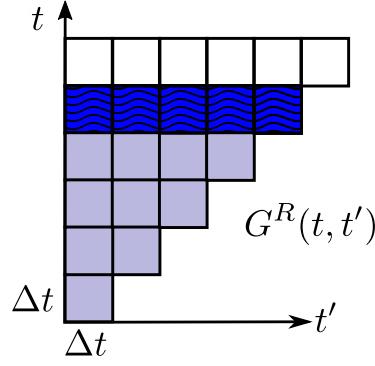
Fig. 3: *Illustration of the integral equation* (46): *The hatched region indicates a time-slice* $\{\,G^R(n\Delta t, m\Delta t)\,|\,m\leq n\,\}$. *The blue region indicates the values of* G^R *entering the evaluation of the derivative* $\partial_t G^R(t,t')$ *which is needed to propagate* G^R *from a time-slice* $m\Delta t$ *to* $(m+1)\Delta t$.

(for other implementations, see, e.g., [34]):

$$\big(-\partial_\tau - h(0^-)\big)G^M(\tau) - \int_0^\beta d\bar{\tau}\,\Sigma^M(\tau-\bar{\tau})\,G^M(\bar{\tau}) = \delta(\tau), \tag{49}$$

$$\big(i\partial_t - h(t)\big)\,G^R(t,t') - \int_{t'}^t d\bar{t}\,\Sigma^R(t,\bar{t})\,G^R(\bar{t},t') \quad = \delta(t-t'), \tag{50}$$

$$\big(i\partial_t - h(t)\big)\,G^{t v}(t,\tau') - \int_0^t d\bar{t}\,\Sigma^R(t,\bar{t})\,G^{t v}(\bar{t},\tau') \quad = Q^{t v}(t,t'), \tag{51}$$

$$\big(i\partial_t - h(t)\big)\,G^<(t,t') - \int_0^t d\bar{t}\,\Sigma^R(t,\bar{t})\,G^<(\bar{t},t') \quad = Q^<(t,t'), \tag{52}$$

with

$$Q^{t v}(t,\tau') = \int_0^\beta d\bar{\tau}\,\Sigma^{t v}(t,\bar{\tau})\,G^M(\bar{\tau},\tau'), \tag{53}$$

$$Q^<(t,t') = \int_0^{t'} d\bar{t}\,\Sigma^<(t,\bar{t})\,G^A(\bar{t},t') - i\int_0^\beta d\bar{\tau}\,\Sigma^{t v}(t,\bar{\tau})\,G^{v t}(\bar{\tau},t'). \tag{54}$$

Here, the integral limits take into account that retarded functions vanish for $t < t'$, $X^{v t}(\tau,t) = X(-i\tau, t_\pm)$. The component with both time arguments on the imaginary branch is the usual initial state Matsubara Green function, $X(-i\tau, -i\tau') \equiv iX^M(\tau-\tau')$. These integral equations and the equivalent conjugate equation $G * G^{-1} = 1$ for the real and imaginary time Green functions are known as Kadanoff-Baym equations [34]. Apparently Eq. (49) for G^M is decoupled from the other equations. It can be solved in advance to give the Matsubara Green function of the initial equilibrium state, which then enters the other equations in the form of an initial conditions.

If no cutoff to the memory integrals is applied, the required computational resources scale with the number of time-steps M like $\mathcal{O}(M^3)$ (CPU time) and $\mathcal{O}(M^2)$ (memory), which can provide a bottleneck for the simulation, in particular in case of many orbitals.

2.4   Steady-state formalism

In a time-translationally invariant non-equilibrium steady state, the Kadanoff-Baym equations can be solved by means of Fourier transform. The imaginary time branch, which corresponds to the initial state correlations, is moved to $t_0 = -\infty$ and then omitted. The individual components of Eq. (45) become

$$G^R(\omega + i0) = \big(\omega + i0 - h - \Sigma^R(\omega + i0)\big)^{-1} = G^A(\omega - i0)^\dagger, \tag{55}$$

$$\big(\omega + i0 - h - \Sigma^R(\omega + i0)\big) G^K(\omega) = \Sigma^K(\omega)\, G^A(\omega). \tag{56}$$

The second equation can thus be solved as

$$G^K(\omega) = G^R(\omega)\, \Sigma^K(\omega)\, G^A(\omega). \tag{57}$$

In practice, one can iteratively solve Eqs. (55) and (57) together with a given approximation $\Sigma[G]$ for the self-energy, such as Eq. (34): Starting from a given guess for $\Sigma^R(\omega + i0)$ and $\Sigma^K(\omega)$, $G^K(\omega)$, $G^R(\omega + i0)$, and the spectral function $A(\omega)$ are obtained. A Fourier transform gives $G^R(t) = -i\theta(t)\int d\omega\, A(\omega)\, e^{-i\omega t}$ and $G^K(t) = \int \frac{d\omega}{2\pi}\, G^K(\omega)\, e^{-i\omega t}$, which are then used to calculate $\Sigma^R(t)$ and $\Sigma^K(t)$, and thus $\Sigma^R(\omega + i0)$ and $\Sigma^K(\omega)$. The procedure is iterated to convergence. Since the components $A(\omega)$, $\Sigma^K(\omega)$, $G^K(\omega)$ are well localized in frequency, the frequency grid can be kept finite.

The solution of Eq. (57) is not unique for $\Sigma = 0$, i.e., for a noninteracting system in isolation from the environment: In this case, Eq. (56) is solved by any ansatz of the form

$$G_0^K(\omega) = G^R(\omega)\, F(\omega) - F(\omega)\, G^A(\omega), \tag{58}$$

with an arbitrary (hermitian) distribution function $F(\omega)$. This fact just shows that for an isolated noninteracting system any distribution of the single-particle levels provides a possible steady state. By extending the real-time part of the contour to $(-\infty, \infty)$ the memory on the initial condition has been removed, which thus leaves the steady state undetermined for $\Sigma^K = 0$. One can resolve this ambiguity by fixing the distribution function in the solution Eq. (58) of Eq. (56). Mathematically, this is achieved by a choice $\Sigma^K(\omega) = -i\eta F(\omega)$ with $\eta \to 0^+$, which corresponds to attaching a heat bath to the system with a flat density of states, a given distribution $F(\omega)$, and infinitesimal coupling $\sqrt{\eta}$. In the steady state the bath determines the distribution function of the system, irrespective of the coupling strength, while the spectral properties of the system are not affected.

3   Non-equilibrium dynamical mean-field theory

3.1   The dynamical mean-field formalism

DMFT approximates only the spatial correlations in a mean-field manner, but accurately treats local temporal fluctuations. The main approximation is the locality of the self-energy, which becomes exact in the limit of infinite coordination number [35]. The formulation of DMFT

within the Keldysh and the Matsubara framework differs only by the choice of the time contour, and all arguments regarding the derivation of DMFT, such as the cavity method [20] and power counting arguments for the locality of the self-energy, can be transferred one-to-one from imaginary time to $\mathcal{C}$. We therefore directly state the final equations, and then proceed to a discussion of their solution, which is in fact very different in real and imaginary time.

For clarity, the DMFT equations in this section are all stated for the single-band Hubbard model in the spin-symmetric phase; orbital indices can easily be added. Within DMFT, the self-energy at a given site j of the lattice can be obtained from a local model with a general quadratic action

$$S_{\text{imp},j} = \int_{\mathcal{C}} dt dt' \Big(\sum_{\sigma} \bar{c}_{\sigma}(t)\, \mathcal{G}_{j\sigma}^{-1}(t,t')\, c_{\sigma}(t) - U(t)\, \bar{c}_{\uparrow}(t)c_{\uparrow}(t)\bar{c}_{\downarrow}(t)c_{\downarrow}(t)\, \delta_{\mathcal{C}}(t,t') \Big), \qquad (59)$$

$$\mathcal{G}_{j}^{-1}(t,t') = \big(i\partial_t + \mu\big)\delta_{\mathcal{C}}(t,t') - \Delta_j(t,t'), \qquad (60)$$

which describes one site of the lattice embedded in an environment with hybridization function $\Delta_j(t,t')$. This is the action of a time-dependent Anderson Impurity Hamiltonian. This action defines the interacting impurity Green function

$$G_{\text{imp},j}(t,t') = -i\langle c(t)\bar{c}(t')\rangle_{S_{\text{imp},j}}. \qquad (61)$$

The impurity self-energy is set by the impurity Dyson equation

$$G_{\text{imp},j}^{-1}(t,t') = \mathcal{G}_{j}^{-1}(t,t') - \Sigma_{\text{imp},j}(t,t'). \qquad (62)$$

The impurity self-energy then serves as an approximation for the lattice self-energy,

$$\Sigma_{jj'}(t,t') = \delta_{jj'}\, \Sigma_{\text{imp},j}(t,t'), \qquad (63)$$

and lattice Green functions are obtained by solving the Dyson equation

$$G_{jj'}^{-1}(t,t') = (i\partial_t + \mu)\, \delta_{\mathcal{C}}(t,t')\, \delta_{jj'} - \delta_{jj'}\, \Sigma_{jj}(t,t') - \delta_{\mathcal{C}}(t,t')\, v_{ij}(t), \qquad (64)$$

where $v_{ij}(t)$ are the hopping matrix elements, which contain the external laser fields, Eq. (2). Finally the equations are closed and the auxiliary quantity $\Delta_j(t,t')$ can be eliminated when the local lattice Green function G_{jj} equals the corresponding impurity quantity

$$G_{\text{imp},j}(t,t') \overset{!}{=} G_{jj}(t,t'). \qquad (65)$$

Equations (59) through (65) provide the closed set of equations for non-equilibrium DMFT.

Self-consistency scheme without Σ

In equilibrium, the self-consistent solution of the DMFT equations is usually achieved by an iterative procedure. One can start from a guess for Σ, solve the lattice Dyson equation to obtain G_{ii}, invert the impurity Dyson equation (62) to get Δ, and solve the impurity model with action (59) to get an update for Σ. The same might be done in real time. Although in principle

straightforward matrix equations in time, some of the steps can, however, become numerically unstable, in particular when algorithms are used which are accurate to high-order in the time-step. In particular, given G and Δ one cannot easily solve Eq. (62) for the self-energy. We therefore explain how the self-consistency cycle can be reformulated, avoiding the explicit use of the self-energy. (The following steps are presented for a spatially homogeneous state, where $\varepsilon_{\boldsymbol{k}}(t)$ is the Fourier transform of $v_{ij}(t)$, and $\sum_{\boldsymbol{k}} G_{\boldsymbol{k}}$ is the local Green function. We define the sum to be normalized, $\sum_{\boldsymbol{k}} = 1$.)

(1) Given Δ, G_{imp} is calculated, Eq. (61). This is the main step of the algorithm, which requires the solution of a many-body problem out of equilibrium (Sec. 3.2).

(2) A function Z with $Z^{-1}(t,t') = (i\partial_t + \mu)\,\delta_\mathcal{C}(t,t') - \Sigma(t,t')$ is obtained by solving the integral equation $Z + G_{\text{imp}} * \Delta * Z = G_{\text{imp}}$.

(3) For each $\boldsymbol{k}$, we determine $G_{\boldsymbol{k}}$ from the integral equation $Z + Z * \varepsilon_{\boldsymbol{k}} * G_{\boldsymbol{k}} = G_{\boldsymbol{k}}$. (Here $\varepsilon_{\boldsymbol{k}}(t,t') \equiv \varepsilon_{\boldsymbol{k}}(t)\,\delta_\mathcal{C}(t,t')$ is interpreted as diagonal matrix in time.)

(4) We calculate the sums $G = \sum_{\boldsymbol{k}} G_{\boldsymbol{k}}$, $G_1 = \sum_{\boldsymbol{k}} \varepsilon_{\boldsymbol{k}} * G_{\boldsymbol{k}}$, $G_2 = \sum_{\boldsymbol{k}} (\varepsilon_{\boldsymbol{k}} + \varepsilon_{\boldsymbol{k}} * G_{\boldsymbol{k}} * \varepsilon_{\boldsymbol{k}})$, and obtain Δ from the integral equation $\Delta + G_1 * \Delta = G_2$.

These equations are obtained directly by summing the lattice Dyson equation over $\boldsymbol{k}$ and comparing to the impurity Dyson equation. Steps (2)–(4) require the solution of linear equations on $\mathcal{C}$ of the form $(1 + F) * X = Q$, with a kernel F and a source term Q. Such equations reduce to stable second-order Volterra equations in time [32, 33]. Because all these steps are causal (the solution in some domain $t,t' \le t_0$ can be determined from the input in the same domain $t,t' \le t_0$) the real-time DMFT equations can be propagated step by step in time.

We finally note that, while in equilibrium momentum sums can be rewritten in terms of integrals over the density of state, $\sum_{\boldsymbol{k}} = \int d\varepsilon\, D(\varepsilon)$ with $D(\varepsilon) = \sum_{\boldsymbol{k}} \delta(\varepsilon - \varepsilon_{\boldsymbol{k}})$, this is not necessarily possible when $\varepsilon_{\boldsymbol{k}}$ is time-dependent, because in this case $G_{\boldsymbol{k}}(t,t')$ depends on $\boldsymbol{k}$ not only via a single number such as the unperturbed $\varepsilon_{\boldsymbol{k}}^0$ [e.g., with a vector-potential $\boldsymbol{A}(t)$, Eq. (2) implies $\varepsilon_{\boldsymbol{k}}(t) = \varepsilon_{\boldsymbol{k}+e\boldsymbol{A}(t)}$].

Bethe lattice

The solution of an integral equation for each $\boldsymbol{k}$, i.e., step (3) in the self-consistency above, can be numerically costly. For predictions of DMFT which should be generic for any lattice, one can therefore use the so-called Bethe lattice, which leads to a closed-form self-consistency. This is also common in equilibrium DMFT, but with a slight variation even electric fields can naturally be included: The Bethe lattice is a graph with coordination number Z, but no loops. As for any tight-binding model, the electric field is defined on the links (ij) of the graph by means of the Peierls phase $e^{\pm i\phi_{ij}(t)}$, so that $\phi_{ij}(t) = eaA_{ij}(t)$, where $aA_{ij}(t)$ is the projection of the vector potential along the bond. To have a divergence-less field on this graph, each site should simply have equally many bonds with a field pointing inwards and pointing outwards.

In general, a formal closed form self-consistency is obtained from the cavity construction [20] (integrating out the rest of the lattice), which gives

$$\Delta_j(t,t') = \sum_{j_1,j_2} v_{j,j_1}(t)\, G^{[j]}_{j_1,j_2}(t,t')\, v_{j_2,j}(t')\,. \tag{66}$$

Here $G^{[j]}_{j_1,j_2}$ is the Green function of the lattice where site j is excluded. On a lattice without loops, only terms $j_1 = j_2$ remain, and in the limit of infinite coordination we then have $G^{[j]}_{j_1,j_1}(t,t') = G_{j_1,j_1}(t,t')$. With half of the hoppings having a phase $e^{i\phi(t)}$ and $e^{-i\phi(t)}$, respectively, and rescaling $v \sim v_*/\sqrt{Z}$ for $Z \to \infty$, a closed-form self-consistency

$$\Delta(t,t') = \frac{v_*^2}{2}\left(e^{i\phi(t)}\, G(t,t')\, e^{-i\phi(t')} + e^{-i\phi(t)}\, G(t,t')\, e^{i\phi(t')} \right) \tag{67}$$

is obtained for a translationally invariant state.

3.2 Impurity solvers

The most challenging part of the DMFT equations is the solution of the auxiliary problem, i.e., the determination of the Green function (61) from the action (59) with a given hybridization function $\Delta(t,t')$. It can be shown that the action (59) describes a time-dependent Anderson impurity Hamiltonian. However, for one reason or the other, it often turns out to be substantially harder to determine the time-evolving non-equilibrium state of a system than determining the equilibrium state. An example are matrix-product states (MPS): While a MPS representation is efficient for ground states which satisfy an area-law entanglement, the time-propagated state can often not be represented efficiently, leading to an exponential increase of computational resources with the simulated time. Quantum Monte Carlo techniques face a different problem with the same devastating effect: Even when a sign-problem can be avoided in equilibrium (imaginary time), summing up all phases in non-equilibrium leads to an exponentially small average sign. It appears that the problem of time-evolution in many body systems is a challenge, although this may seem at odds with the fact that the final state (after thermalization) is again simple. So far, all impurity solvers are therefore restricted to either short times, or rely on approximations which work in certain regimes of parameter space only.

Weak-coupling expansions of the self-energy

In equilibrium and for the half-filled single-band Hubbard model, second-order perturbation theory (iterated perturbation theory, IPT) extrapolates between weak and strong coupling when it is formulated in terms of the bare Green function (60), and qualitatively reproduces the metal-insulator transition [20]. In non-equilibrium, IPT has so far remained restricted to the weak-coupling regime, because the non-conserving nature of the bare expansion can lead to artifacts in the time-evolution [33]. Apart from that, weak-coupling approximations are easy to implement, cf. Eq. (34), and numerically relatively cheap.

Quantum Monte Carlo techniques

In equilibrium, quantum Monte Carlo (QMC) can give numerically exact results at nonzero temperature [36]. QMC stochastically sums the perturbation expansion in the hybridization function or the interaction to all orders. In real-time, the contributions to the perturbation expansion become complex-valued, which results in a dynamical sign problem and limits a straight-forward real-time generalization of the imaginary-time QMC to short times. There are interesting and fundamental problems to be studied in the short-time dynamics, such as dynamical phase transitions [18], but in order to study the photo-induced dynamics in most materials few hopping times are often not yet sufficient. Recent developments which indicate ways to overcome the dynamical sign-problem [37] have not been tested in the context of non-equilibrium DMFT.

Hamiltonian representation of the impurity problem

If one can find a finite system which can accurately reproduce a given hybridization function $\Delta(t, t')$, the Green function can be determined from a numerical solution of the time-dependent Schrödinger equation, such as using matrix product states and the density matrix renormalization group [38]. It can be shown that a general action with hybridization $\Delta(t, t')$ is indeed representable by an Anderson impurity model in the most simple geometry, i.e., a star-geometry where the impurity site is coupled to bath sites but there is no link between the bath sites [39]. In this representation, the number of bath orbitals which are needed increases with the simulated time, leading a exponential increase of the computation time. So far, this approach has been used only for the special situation in which the initial state consists of a lattice of uncoupled sites (this is a quench situation which can be realized in cold atoms), but in principle more general initial states can be included. A different representation has been derived for the steady state, using an impurity model in which the bath-sites are coupled to dissipative Lindblad terms [40]. In general, the numerical effort in the Hamiltonian-based techniques increases exponentially with the number of orbitals, which limits the frequency resolution in the steady state and the accessible times in the real-time formalism.

Perturbation theory in the hybridization function

A systematic expansion in $\Delta(t, t')$, with the atomic limit as zeroth order, is expected to work well in the Mott phase, it can be formulated for an arbitrary local part of the Hamiltonian (multi-orbital Hubbard models, electron-phonon interactions), and one can re-sum the terms of the expansion in such a way that the theory becomes conserving. In particular the lowest order (the so called non-crossing approximation, NCA) has been used extensively to study the dynamics of Mott insulators within DMFT. In the following we summarize the equations for the NCA. The technical details of this expansion on the Keldysh contour are explained in Ref. [41] and Ref. [24], to which we also refer for a list of early references related to the use of the expansion as an impurity solver for DMFT and cluster DMFT in equilibrium.

In the hybridization expansion one splits the action S into the local part $S_{at} = \int_{\mathcal{C}} dt\, H_{at}(t)$, where the atomic Hamiltonian H_{at} contains the local interaction, and the hybridization S_{Δ}. The latter can have a very general form, such as

$$S_{\Delta} = -\sum_{\gamma} \int_{\mathcal{C}} dt_1 dt_2\, \bar{\phi}_{\gamma}(t) \Delta_{\gamma}(t, t')\, \psi_{\gamma}(t'), \tag{68}$$

where γ sums over all hybridization channels, and ψ and $\bar{\phi}$ are quite general operators. In the single impurity Anderson model, e.g., $\gamma \equiv \sigma$, $\bar{\phi}_{\gamma} \equiv \bar{c}_{\sigma}$, $\psi_{\gamma} \equiv c_{\sigma}$, but the general formulation also allows for inter-orbital hybridizations in multi-band systems with spin-orbital indices a, a', such as $\sum_{a,a'} \int_{\mathcal{C}} dt_1 dt_2\, \bar{c}_a(t) \Delta_{aa'}(t, t')\, c_{a'}(t')$, where $\gamma \equiv (a, a')$, anomalous hybridizations in superconducting systems, $\int_{\mathcal{C}} dt_1 dt_2 \left[c_{\uparrow}(t) \Delta_{cc}(t, t') c_{\downarrow}(t') + \bar{c}_{\downarrow}(t) \Delta_{\bar{c}\bar{c}}(t, t') \bar{c}_{\uparrow}(t') \right]$, retarded density-density interactions $\sum_{\sigma\sigma'} \int_{\mathcal{C}} dt_1 dt_2\, n_{\sigma}(t) V_{\sigma,\sigma'}(t, t') n_{\sigma}(t')$ (here $\bar{\phi}_{\sigma,\sigma'} \equiv \bar{c}_{\sigma} c_{\sigma}$ and $\psi_{\sigma,\sigma'} \equiv \bar{c}_{\sigma'} c_{\sigma'}$), or electron-phonon interactions ($\psi = c_{\sigma} b, c_{\sigma} \bar{b}$ etc., acting in a local space of electrons and phonons).

The hybridization expansion is formulated in terms of propagators of the many-body states $|\alpha\rangle$ of the isolated impurity. For example, for the single-impurity model, these are the Fock-states $|0\rangle$, $c_{\uparrow}^{\dagger}|0\rangle$, $c_{\downarrow}^{\dagger}|0\rangle$, $c_{\downarrow}^{\dagger} c_{\uparrow}^{\dagger}|0\rangle$. In the hybridization expansion, we introduce bare propagators $g_{\alpha\alpha'}(t, t')$ and renormalized propagators $\mathcal{G}_{\alpha,\alpha'}(t, t')$, which capture the propagation from state α' to α along the forward direction on $\mathcal{C}$. The zeroth order propagators are just the time-evolution operators of the atomic Hamiltonian

$$g_{\alpha,\alpha'}(t, t') = -i\langle\alpha| T_{\mathcal{C}}\, e^{-i\int_{\mathcal{C}, t'}^{t} d\bar{t}\, H_{at}(\bar{t})} |\alpha'\rangle \qquad \text{for } t >_{\mathcal{C}} t', \tag{69}$$

$$g(t, t') = i g(t, 0_+)\, \xi\, g(-i\beta, t') \qquad \text{for } t <_{\mathcal{C}} t'. \tag{70}$$

The second line specifies how to "glue" together propagators along the open end of the contour (g is understood as a matrix in α, α'), such that the evolution direction is always in forward direction along $\mathcal{C}$: For $t <_{\mathcal{C}} t'$, the propagation from t' to t along $\mathcal{C}$ involves a propagation to the end $-i\beta$ of $\mathcal{C}$, and then a propagation form 0_+ to t (see Fig. 4a). The matrix $\xi_{\alpha\alpha'} = \delta_{\alpha\alpha'}(-1)^{n_{\alpha}^F}$, where n_{α}^F is the number of Fermions in $|\alpha\rangle$, is introduced for convenience so that g satisfies the boundary condition (27) for bosons and fermions if there is an even and odd number of fermions in α, respectively. (Note that g, and later $\mathcal{G}$ are at least block-diagonal with respect to the Fermion number, i.e., ξ commutes with $\mathcal{G}$.)

The renormalized propagators $\mathcal{G}(t, t')$ simply include all hybridization events between t' and t in forward direction along $\mathcal{C}$. When the time-evolution operator $e^{iS_{at}+iS_{\Delta}}$ is expanded in S_{Δ}, these terms can be represented intuitively as diagrams as shown in Fig. 4c. All diagrams can be re-summed into a Dyson series, which takes the form

$$\mathcal{G} = g + g \odot \Sigma \odot \mathcal{G}, \tag{71}$$

where Σ (also a matrix in α) contains all topologically connected hybridization diagrams, and the convolution $\odot$ is understood as a time-ordered convolution along forward direction on $\mathcal{C}$
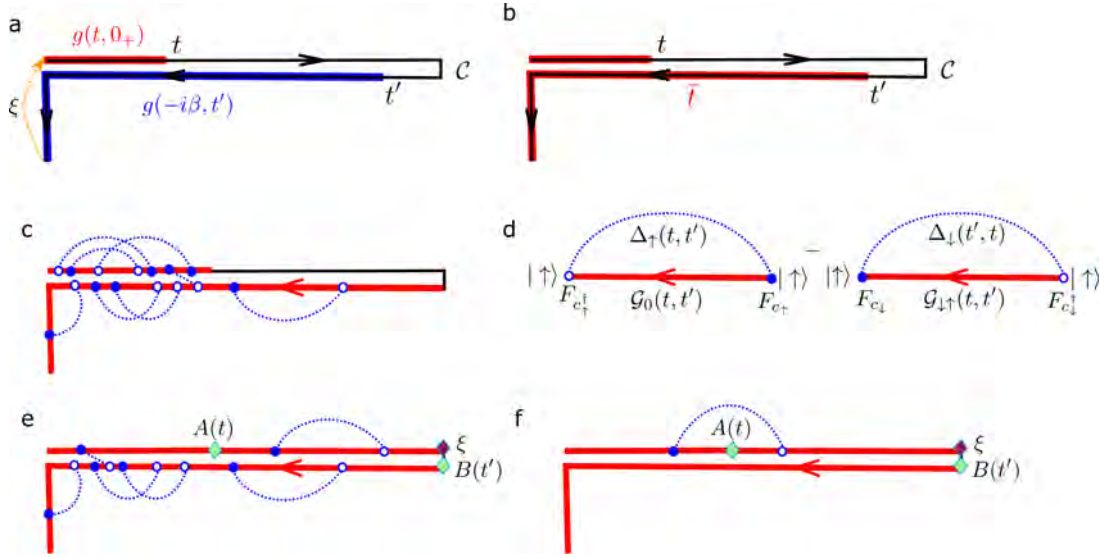
Fig. 4: *Illustration of the hybridization expansion: (a) gluing together time-evolution operators along the contour in a cyclic fashion. (b) The integration range of the convolution $\odot$ along $\mathcal{C}$, cf. Eqs. (72) and (73) (c) Diagrams contributing to $\mathcal{G}$, where the blue dotted lines represent $\Delta(t, t')$, the open/filled lines are the vertex operators F_ψ, $F_{\bar\phi}$, and the red lines represent g (d) The diagrams for the NCA self-energy $\Sigma_{|\uparrow\rangle}$ in the single-impurity Anderson model. (e) Diagrams for the correlation function $\langle A(t)B(t')\rangle_S$ without (e) and with (f) vertex corrections.*

(Fig. 4b):

$$[A \odot B](t,t') = \int_{\mathcal{C}:t>_\mathcal{C}\bar{t}>_\mathcal{C}t'} d\bar{t}\, A(t,\bar{t})B(\bar{t},t') \qquad \text{for } t >_\mathcal{C} t' \qquad (72)$$

$$[A \odot B](t,t') = \int_{\mathcal{C}:-i\beta>_\mathcal{C}\bar{t}>_\mathcal{C}t'} d\bar{t}\, A(t,\bar{t})B(\bar{t},t') + \int_{\mathcal{C}:t>_\mathcal{C}\bar{t}>0_+} d\bar{t}\, A(t,\bar{t})B(\bar{t},t') \qquad \text{for } t <_\mathcal{C} t. \qquad (73)$$

Such time-ordered convolutions naturally appear in the expansion of the time-evolution operator. In practice, using the differential equation for the evolution operator one can solve the Dyson equation (71) as an integral-differential equation

$$\left(i\partial_t - H_{at}\right)\mathcal{G}(t,t') - [\Sigma \odot \mathcal{G}](t,t') = 0, \qquad (74)$$

to be solved with the initial condition $\mathcal{G}(t_-,t+) = -i$, and the boundary condition (27). By construction, the trace

$$Z = \mathrm{Tr}\left(\xi\, i\mathcal{G}(t_+,t_-)\right) \qquad (75)$$

is the partition function. In the following, we assume that $Z = 1$, which can always be achieved by adding a suitable constant to H_{at}). $R = \xi\, i\mathcal{G}(t_+,t_-)$ is the reduced density matrix on the impurity, $R_{\alpha\alpha'} = \mathrm{Tr}_{\mathrm{bath}}[|\alpha'\rangle\langle\alpha|]$, so that all local observables on the impurity are obtained from

$$\langle\hat{O}\rangle = \mathrm{Tr}\left(\xi\, i\mathcal{G}(t_+,t_-)\,\hat{O}\right), \qquad (76)$$

once the propagators $\mathcal{G}$ are known.

In the non-crossing approximations, one considers only hybridization diagrams without crossings (also crossings between lines of different flavor Δ_γ are excluded). This can be understood as a leading order expansion in the self-consistent diagrammatic expansion which can be derived from a Luttinger-Ward functional and thus leads to a conserving approximation. The diagrams have a simple form, where for each channel γ in Eq. (68) one adds two diagrams for the two directions of Δ,

$$\Sigma(t,t') = \sum_\gamma i\Big(\Delta_\gamma(t,t')\, F_{\bar\phi_\gamma}(t)\, \mathcal{G}(t,t')\, F_{\psi_\gamma}(t') + P_\gamma\, \Delta_\gamma(t',t)\, F_{\psi_\gamma}(t)\, \mathcal{G}(t,t')\, F_{\bar\phi_\gamma}(t') \Big), \quad (77)$$

where $(F_A)_{\alpha\alpha'} = \langle \alpha |A| \alpha' \rangle$ is the matrix representation of the vertex operators $A = \psi_\gamma, \bar\phi_\gamma$, and $P_\gamma = -1$ if ψ_γ and $\bar\phi_\gamma$ are fermionic operators. These diagrams have an intuitive interpretation, where the vertex operators corresponds to a simultaneous transition between a many-body state on the impurity and a transition in the bath. For example, the first diagram in Fig. 4d shows the emission of an electron with spin $\uparrow$ in the bath, causing a transition of the impurity state from $|\uparrow\rangle$ to $|0\rangle$. The electron then propagates in the bath and is later reabsorbed.

Finally, in addition to observables (76) one needs contour-ordered two-point correlation functions $\langle T_\mathcal{C} A(t)B(t')\rangle_S$. The operators can simply be inserted as additional vertices on the contour. The general diagrammatic series contains the bare term

$$\langle T_\mathcal{C} A(t)B(t')\rangle_S = -\, \mathrm{Tr}\left(\xi\, \mathcal{G}(t',t)\, F_A(t)\mathcal{G}(t,t')\, F_B(t') \right). \qquad (78)$$

One may check the consistency of this term with Eq. (76) (using $\mathcal{G}(t_-,t_+) = -i$)

$$\langle T_\mathcal{C} A(t_-)B(t_+)\rangle_S = -\,\mathrm{Tr}\left[\xi\mathcal{G}(t_+,t_-) F_A \mathcal{G}(t_-,t_+) F_B \right] = i\,\mathrm{Tr}\left[\mathcal{G}(t_+,t_-)\xi F_{AB} \right] \overset{(76)}{=} \langle A(t)B(t)\rangle$$

$$\langle T_\mathcal{C} A(t_+)B(t_-)\rangle_S = -\,\mathrm{Tr}\left[\xi\mathcal{G}(t_-,t_+) F_A \mathcal{G}(t_+,t_-) F_B \right] = i\,\mathrm{Tr}\left[\xi F_A \mathcal{G}(t_+,t_-) F_B \right] =$$

$$= i\,\mathrm{Tr}\left[\mathcal{G}(t_+,t_-) F_B \xi F_A \right] = \pm i\,\mathrm{Tr}\left[\mathcal{G}(t_+,t_-) F_B F_A \xi \right] = \pm\langle B(t)A(t)\rangle.$$

Here we have used that the matrix ξ commutes with $\mathcal{G}$, because the evolution conserves the Fermion parity, and it commutes (anti-commutes) with the matrix F_X if X is a Bose (Fermi) operator. One can also verify Eq. (78) in the atomic limit, using Eqs. (69) and (70). Eq. (78) is used in the NCA impurity solver to measure the impurity Green function. Equations (74), (77), and (78) thus provide the complete set of equations for the most general multi-orbital NCA. The equations have a matrix structure with the Fock-space dimension of the impurity, but symmetries usually render these equations block-diagonal, at least in the fermion parity, and for non-superconducting states also in the particle number.

We note that in general the expectation value $\langle T_\mathcal{C} A(t)B(t')\rangle_S$ contains diagrams which correspond to vertex corrections of the operators A and B, see Fig. 4e and f. Even within NCA, some of these diagrams are generated if the correlation function $\langle T_\mathcal{C} A(t)B(t')\rangle_S$ is calculated by explicitly taking a derivative of the NCA solution to $\langle B(t')\rangle_S$ with respect to a source field that couples to $A(t)$. Such an explicit measurement, which includes the vertex corrections, can be useful for the calculation of susceptibilities within NCA. For the measurement of the Green function within the DMFT cycle, one sticks to Eq. (78), which gives a consistent approximation.

4   Photo-doping the Mott insulator

The Mott transition, at which electrons get localized due to the Coulomb interaction, is one of the hallmarks of strong electronic correlations in solids. In contrast to a band-insulator with filled or empty bands, electrons in the Mott insulator still have active spin and orbital degrees of freedom, which can result in complex phases with magnetic and orbital order. Short-ranged magnetic and orbital correlations, on the other hand, may induce interactions between doped electrons and holes, and thus give rise to yet new states such as superconductivity. The development of DMFT has been instrumental in the understanding of the Mott transition [21], and it is therefore a natural application of the non-equilibrium extension of DMFT to analyze the dynamics of Mott insulators after various excitation protocols.

4.1   Paramagnetic Mott insulator

The most straightforward way to excite a Mott insulator is a short electric field pulse of frequency $\Omega \approx U$. This generates charge excitations in the paramagnetic Mott insulator, i.e. doubly occupied and empty sites. The properties of such a photo-excited state and its thermalization have been analyzed in Ref. [42]. Figure 5a) shows the time-evolution of the double occupancy $d(t) = \langle n_\uparrow(t) n_\downarrow(t) \rangle$ during and after the excitation. These results have been obtained for the Bethe lattice and the NCA impurity solver, using a single-cycle electric-field pulse. Setting the bandwidth $W = 4$ fixes the energy- and timescale ($\hbar = 1$). (The results in [42] have been obtained for the hyper-cubic lattice using the hybridization expansion up to third order. They are qualitatively similar to the results shown here.)

The double occupancy increases during the pulse, and subsequently shows an exponential relaxation to a new final value. Thermalization would imply that the properties of the system eventually approach the properties of a system in equilibrium, at a temperature T_f such that the total energy equals the thermal energy expectation value $E_{th}(T_f)$ at temperature T_f, $\langle H(t) \rangle \equiv E_{tot} \overset{!}{=} E_{th}(T_f)$. (Note that the system is treated in isolation from environment, so that the total energy is conserved after the excitation. We can determine T_f from a comparison to independent equilibrium simulations, and then compute the thermal expectation value $d_{th}(T_f)$ for the different values of U in Fig. 5. A fit of the form

$$d(t) = d_{th}(T_f) + A \exp(-t/\tau), \tag{79}$$

(see black dashed lines) shows that the evolution of $d(t)$ is compatible with thermalization of the electronic system. The timescales, however, strongly depend on U, and range from few hopping times in the correlated metal ($U = 2.5$), to $\tau > 1000$ in the Mott phase ($U = 6$). Empirically, the dependence of the thermalization times on U can be described by the exponential dependence $\tau(U) \sim \exp\left[\alpha \frac{U}{v_*} \log\left(\frac{U}{v_*}\right)\right]$, with some numerical constant α (blue dashed line in Fig. 5b). This result has an interpretation in terms of a bottleneck due to the inefficient transfer of a large energy quantum of order U into many single-particle excitations [43]. The exponential dependence was first measured in a system of ultra-cold atoms [43]. In solids, the life-times
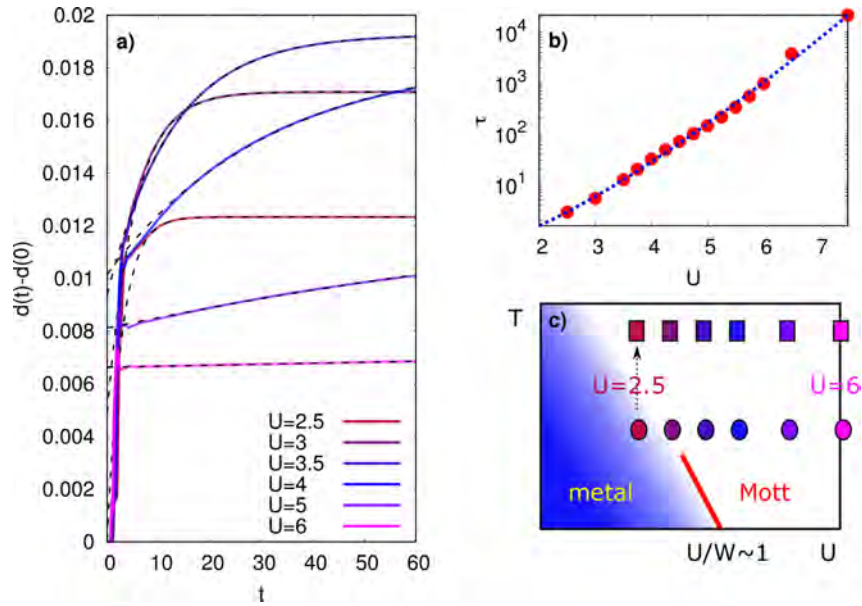
Fig. 5: *a) Evolution of the double occupancy in the Hubbard model on the Bethe lattice during and after a single-cycle pulse of duration $2\delta t$ with $\delta t = 2\pi/\Omega$ and $\Omega = U$, i.e., $A(t) = A_0 e^{-4(t-\delta t)^2/\delta t^2} \sin(t-\delta t)\Omega$ for $0 \le t \le 2\delta t$ in Eq. (67). The initial temperature is $T = 0.2$, initial states correspond to values of U in the metal-insulator crossover and in the Mott state, as schematically shown by the circle symbols in panel c). Square symbols in c) show the state after thermalization ($T_f \approx 0.5$ for all curves). Dashed lines in a) are exponential fits, see Eq. (79). b) Symbols: Relaxation times τ, obtained from the fits (79).*

of photo-excited carriers in Mott insulators can indeed range to thousands of hopping times (picoseconds), but the decay mechanism may involve other degrees of freedom: Spin-fluctuations have been discussed as a possible mechanism for the doublon decay in cuprates [44, 45], while in organic materials there are molecular vibrations at relatively high energies ω_0, opening the possibility for a multi-phonon decay at a timescale governed by U/ω_0 rather than U/W [46, 47].

Thermalization of small-gap Mott insulators

We now focus on the regime of small U, where rapid thermalization is observed in the double occupancy. We can identify the thermalization also in the relaxation of the spectral function and the occupation function, see Fig. 6. In the Figure, the spectral function and occupation function have been obtained by the backward Fourier transform with cutoff s_{max}

$$A(\omega, t) = -\frac{1}{\pi} \operatorname{Im} \int_0^{s_{max}} ds\, G^R(t, t-s)\, e^{i\omega s} \tag{80}$$

$$N^<(\omega, t) = -\frac{1}{\pi} \operatorname{Im} \int_0^{s_{max}} ds\, G^<(t, t-s)\, e^{i\omega s}. \tag{81}$$

(The Wigner transform, or a photoemission spectrum (10) would look similar.) Both spectral function and occupation function become independent of t within a few hopping times, comparable to the relaxation time τ of the double occupancy. At the latest time $t = 18$, we find
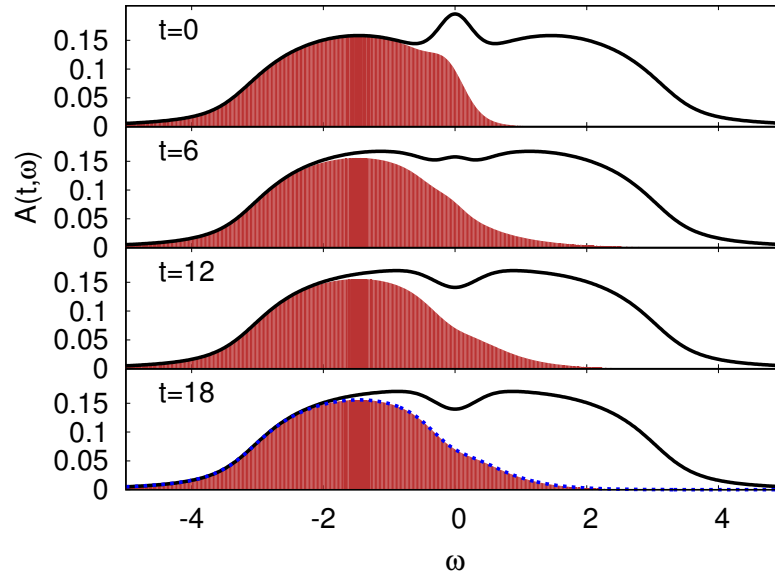
Fig. 6: *a) Spectral function, Eq. (80), for $U = 2.5$, $\beta = 5$ and the same excitation protocol as in Fig. 5, plotted for different times t. The shaded region shows the occupation function, Eq. (81), for the same parameters. The blue dotted line for $t = 18$ shows $A(t, \omega) f(\omega, T_f)$, where $T_f = 1/1.967$ is determined from the total energy.*

the fluctuation theorem satisfied in the form $N^<(\omega) = A(\omega) f(\omega, T_f)$, with the temperature $T_f = 1/1.967$ is obtained from the total energy. This confirms that, regarding the single-particle properties, the system indeed thermalizes on the timescale of few hoppings.

A rapid thermalization of a small-gap Mott insulator is in agreement with early time-resolved photoemission measurements on the Mott insulator 1T-TaS$_2$ [48]. At the shortest measurable times, the spectrum of the photo-excited system resembles that of a Mott insulator at electronic temperatures of the order of the gap, where thermal effects lead to a filling in of states in the gap. In spite of some naive expectation, rapid thermalization of a strongly correlated system is far from obvious: Already the analysis above predicts a rather sensitive dependence of the thermalization time on the gap, and also model studies for an interaction quench in the Hubbard model [18] show thermalization within timescales of the order of the bandwidth only in a narrow interaction regime. Most importantly, thermalization in a strongly correlated system cannot directly be understood from a simple Boltzmann equation. The latter would only describe the evolution of the occupation function, while thermalization in the correlated system implies that also the spectral function is modified. In Fig. 6, e.g., the spectral function completely changes during the evolution: In the initial state ($\beta = 5$) there is still a reminiscence of the quasiparticle peak, while in the final state at high electronic temperature the system resides in a bad-metallic state, with a pseudo-gap instead of the quasiparticle peak.

In view of this, it is reassuring that recently also a successful comparison between theory and experiment of time-dependent features of the thermalization could be achieved [49]. A refined analysis of the photoemission spectroscopy in 1T-TaS$_2$ shows the transient emergence and decay of the population in the upper Hubbard band. Such a reduction of the occupied weight in the upper band should happen along with the electronic thermalization if the system is slightly hole-
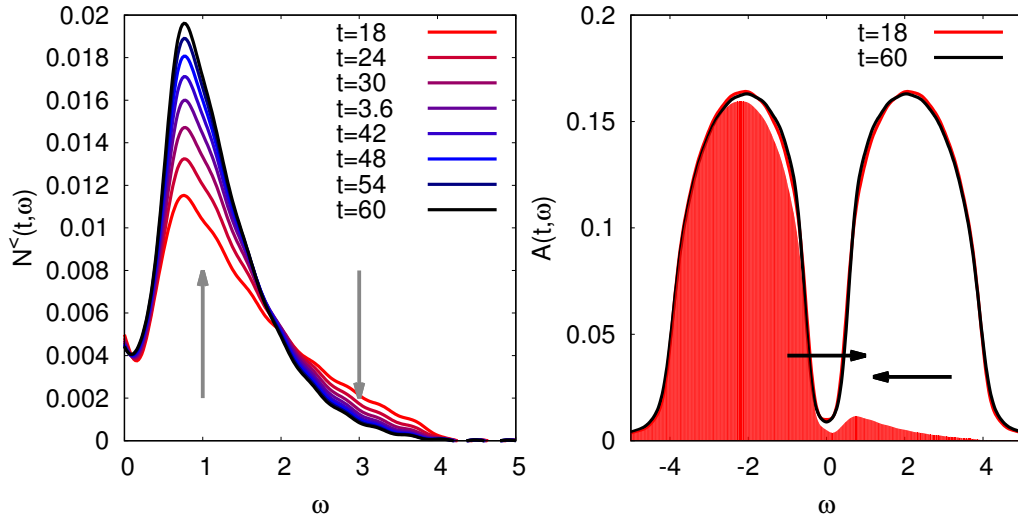
Fig. 7: *a) Occupation function, Eq. (81), for $U = 4$ and the same excitation protocol as in Fig. 5, plotted for different times t. The arrows indicate increase and decrease of weight at low and high energies, respectively. b) Spectral function, Eq. (80), for the same parameters. The arrows indicate an energy-conserving redistribution of occupied weight, as approximately described by a local Boltzmann equation (see text).*

doped. Since the laser transfers population both within the Hubbard bands and to higher and lower bands other than the valence band, the filling in the valence band may change during the excitation. In spite of the extremely sensitive dependence of thermalization timescales on the model parameters, the observed experimental bound for this timescale is consistent with DMFT results [49].

Impact ionization

In Fig. 5 one can see that the double occupancy increases during the thermalization after the pulse. This implies that the kinetic energy of the photo-excited state is initially too high, and kinetic energy from one or more charge excitations is used to generate *additional doublons*. This process is similar to an Auger process in atomic physics, or *impact ionization* in semiconductors [50]. The process is visible also in the evolution of the occupation function (Fig. 7a). The occupied density of states (81) in the upper Hubbard band shows an increase of the weight at small energies, which *exceeds* the decrease at high energies. This phenomenology is clearly distinct from intra-band relaxation via spins and phonons, where the total weight remains constant while it is redistributed from higher to lower energies.

Naively one can argue that a doublon with high kinetic energy (represented by occupied density of states in the upper part of the upper Hubbard band) undergoes a scattering process with a "particle in the lower band" leading to one additional hole (unoccupied weight in the lower Hubbard band) and two doublons with low kinetic energy (occupied density of states in the lower part of the upper Hubbard band), as indicated by the arrows in Fig. 7b. In the ideal case, when the relaxation of each doublon from the high-energy window generates precisely one doublon-hole pair, one would expect the increase of the weight at low energies to be larger

by a factor *three* than the decrease at high energies, a quantitative estimate which works rather well for small gap Mott insulators [50]: In the present case, the increase of weight from $t = 18$ to $t = 60$ in the interval $0.5 \leq \omega \leq 2$ is larger by approximately a factor 3.1 than the decrease in the interval $2 \leq \omega \leq 4$.

The argument presented above seemingly relies on a scattering of quasiparticles (doublons) with a well-defined energy, as described by a Boltzmann equation. The success of such an argument may come as a surprise, as the energy of a doublon is not really well-defined, and the width of the peaks in the momentum-resolved spectral $A_{\mathbf{k}}(\omega)$ function is of order one. However, one can reformulate the scattering argument on the basis of a local time-dependent occupation function defined by $G^{<}(\omega, t) = 2\pi i A(\omega, t) F(\omega, t)$, putting it on more rigorous grounds [51]: Under the assumption that (i), the spectral function $A(\omega)$ is more or less time-independent, which is justified numerically for weakly excited paramagnetic Mott insulators (compare the spectra at the earliest and later time in Fig. 7b), and (ii), that the distribution function $F(\omega, t)$ evolves slowly compared to the inverse bandwidth, one can argue that the non-equilibrium DMFT dynamics of F is given by a local Boltzmann equation

$$
\partial_t F(\omega_1, t) = \alpha \int d\omega_2 d\omega_3 d\omega_4 \, A(\omega_2) A(\omega_2) A(\omega_4) \, \delta(\omega_1 + \omega_2 - \omega_3 - \omega_4) \ \times
$$
$$
\times \ \Big(F(\omega_3) F(\omega_4)(1 - F(\omega_1))(1 - F(\omega_2)) - F(\omega_1) F(\omega_2)(1 - F(\omega_4))(1 - F(\omega_3)) \Big),
$$

where α is a phenomenological parameter. This equation indeed describes energy-conserving scattering processes as shown in Fig. 7b, even though the individual doublons do not have well-defined energies.

Impact ionization processes are interesting in the context of photo-voltaic devices: Usually, a photon creates a single charge excitation, which then quickly relaxes to the bottom of the band due to scattering with phonons. The usable energy per photon is therefore not given by $\hbar\omega$, but only by the gap Δ. However, if impact ionization is faster than such intra-band relaxation processes, the final state can have *two or more* electrons at the energy Δ. DMFT shows that impact ionization processes in small-gap Mott insulators indeed can occur on a time-scale much faster than typical electron-phonon relaxation times. However, as seen below, short-range spin fluctuations in Mott insulators can provide another fast intra-band relaxation mechanism, so that it remains to be seen to what extent impact ionization plays an important role in real Mott materials.

4.2   Dynamics of the antiferromagnetic Mott insulator

At half-filling and on a bipartite lattice, the Hubbard model shows an extended antiferromagnetic phase at low temperature. At weak coupling this phase is well described as a Slater mean-field antiferromagnet, while for large U the Heisenberg model is the limiting description. Several works on DMFT have focused on the melting or partial melting of this phase after photo-excitation or quenches of the interaction. After quenches around large U (Heisenberg regime), there is a threshold of the quench amplitude ΔU beyond which the order rapidly melts [52].
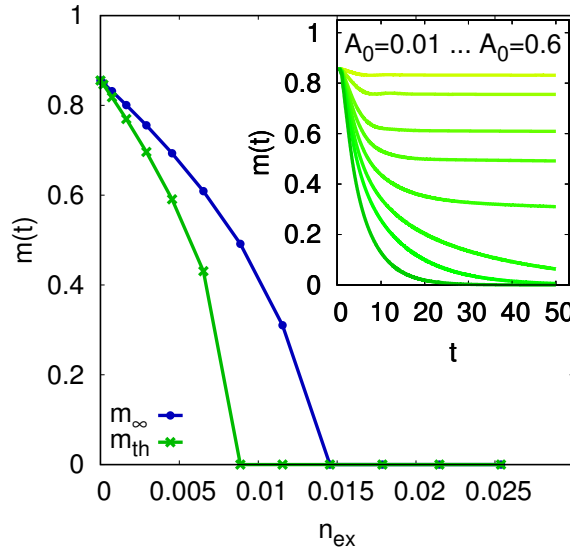
Fig. 8: *Inset: Antiferromagnetic order parameter $m(t)$ in the Hubbard model on the Bethe lattice ($U = 5$, $\beta = 20$), after excitation with a single-cycle electric field pulse. The different curves correspond to different excitation densities (pulse amplitudes A_0) up to $n_{ex} \approx 0.025$. Main plot: Extrapolated value m_∞, obtained by fitting the curves in the inset with $m(t) = m_\infty + Ae^{-\gamma t}$ for $t \geq 15$. m_{th} is the order parameter after thermalization.*

A critical slowdown $1/\tau \sim |\Delta U - \Delta U_c|$ is observed, where ΔU_c is the critical quench amplitude for melting the antiferromagnetic phase. (A similar non-thermal critical behavior is also found after quenches at small interaction [53].) While this reminds of a second-order phase transition, the melting of the anti-ferromagnetism after the quench is a *non-thermal* process: Like the paramagnetic Mott insulator, the antiferromagnetic Mott state thermalizes only on times which are exponentially large in U/W. The ordered state can thus prevail even when the energy after the quench is higher than the energy of the half-filled system *above* the Néel temperature. Instead, the threshold for the melting is set by the number of excited doublons after the quench, i.e., the occupied weight in the upper Hubbard band.

The non-thermal melting can also be seen after excitation with a short pulse: Like in the paramagnetic phase at large U, a pulse leads to an increase of the double occupancy which does not thermalize within the simulated time of ~ 100 hoppings. Figure 8 shows the time-evolution of the antiferromagnetic order parameter $m(t) = \langle c_{j\uparrow}^\dagger c_{j\uparrow} - c_{j\downarrow}^\dagger c_{j\downarrow}\rangle_{j \text{ on } A\text{-sublattice}}$ in the Hubbard model on the Bethe lattice after excitation with an electric field pulse: $m(t)$ saturates to a finite value for excitation densities $n_{ex} \lesssim 0.015$, while complete melting of long-range order is observed for $n_{ex} \gtrsim 0.015$, with a relatively sharp threshold of the final value m_∞ as a function of the excitation density. The corresponding value of the order parameter in the thermalized state, which would be reached after thermalization, $m_{th}(n_{ex})$, is always lower than the value of m_∞ in the photo-excited state. The intermediate state is expected to relax only on the exponentially long timescale of doublon-hole recombination.

The non-thermal melting of the antiferromagnetic order can be understood in terms of a hole which is moving in the antiferromagnetic spin background and thus induces a spin-flip in every hopping process [54]. Because each spin-flip increases the energy in the magnetic sector by
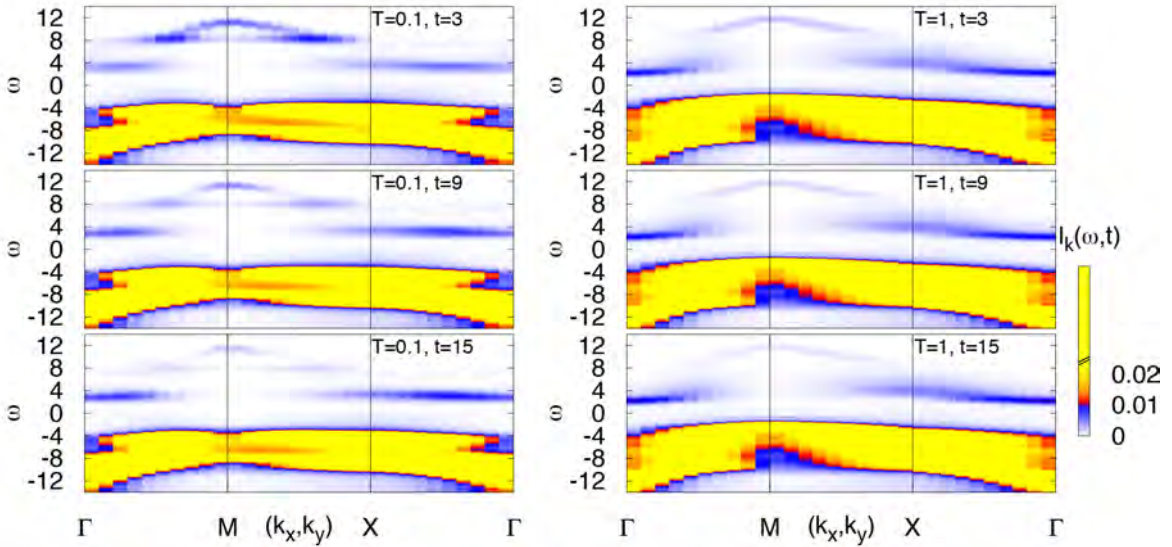
Fig. 9: *Simulated time-resolved photo-emission spectrum in a two-dimensional Mott insulator (Hubbard model, $U = 12$) after a transfer of population to the upper Hubbard band. (Dynamical cluster approximation with a 2×2 cluster and an NCA impurity solver.) At high temperature (right) the relaxation of weight within the upper band becomes slower, because the spins are already thermally disordered ($T \gtrsim J_{ex}$) and cannot take up more energy. Adapted from Ref. [55].*

an amount of the order of the exchange energy $J_{ex} \sim v_*^2/U$, this implies an ultra-fast transfer of kinetic energy from photo-doped electrons to the spins, and thus an ultra-fast mechanism for intra-band relaxation. A rapid energy transfer to spins is even possible in the paramagnetic phase, where spins have no long-range order, but are short-ranged and short-lived. While short-range fluctuations cannot be captured in single-site DMFT, they have been studied using cluster extensions (the dynamical cluster approximation) [55]. Figure 9 shows a simulated time-resolved photo-emission spectrum in the two-dimensional Hubbard model. One finds a redistribution of the occupied density of states, which happens along with a reduction of short-range spin correlations. Using parameters comparable to cuprates, the relaxation times $\tau \sim 10$–20 fs are compatible with the timescales for the initial saturation of the optical response in cuprates after a few-fs laser excitation and with exact-diagonalization results for small clusters in the t-J model [54].

The photo-doped state

In the time window between thermalization (on timescales exponentially large on U/W) and the relaxation of the kinetic energy by partial melting of spin fluctuations, the electronic system is in an almost steady non-equilibrium state. It turns out that in this steady state only the excitation density n_{ex} and the antiferromagnetic order parameter m_∞ remain as the main non-equilibrium control parameters which determine the properties of the system, in analogy to the thermodynamic variables in equilibrium: Firstly, the spectral function of the photo-excited state with given n_{ex} and m_∞ matches the spectral function of a chemically doped system with the same order parameter and a density of carriers $n - 1 = 2n_{ex}$ [52]. This shows that chemically
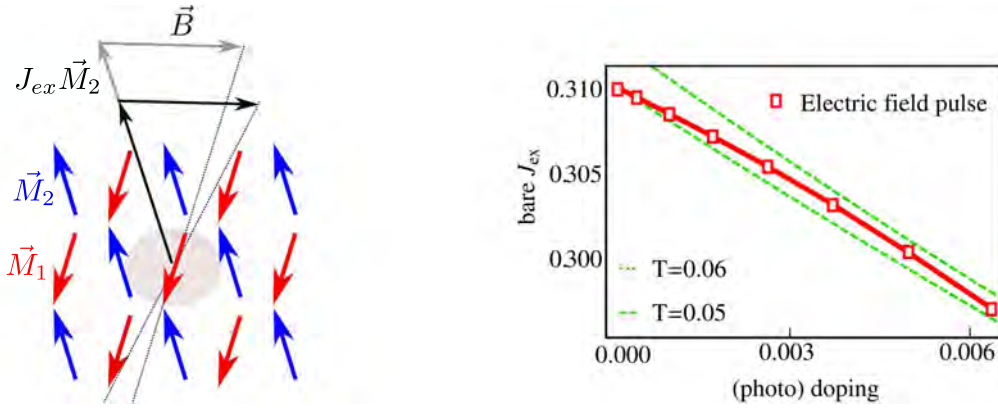
Fig. 10: *Left: Macro-spin dynamics of the antiferromagnetic order parameter after a photo-doping excitation. In the presence of an external field $\boldsymbol{B}$, the order parameter $\boldsymbol{M}_1$ on sub-lattice 1 aligns with the effective field $J_{ex}\boldsymbol{M}_2 + \boldsymbol{B}$. If J_{ex} is modified, a precessional dynamics follows. Right: The exchange interaction extracted from the macro-spin dynamics in the photo-excited system at excitation density $2n_{ex}$ (red symbols), and from the macro-spin state in a chemically doped system with filling $n = 1 + 2n_{ex}$ (green lines). Adapted from Ref. [56].*

doping $n-1$ doublons or holes in equilibrium has a similar effect as photo-exciting the same number of doublons *and* holes, which is why the steady state may be called a photo-doped state. Furthermore, it was shown that also the magnetic exchange interaction J_{ex} is modified in the photo-excited state due to the presence of mobile carriers [56], to the same extent as by chemical doping. The latter can be seen in a time-resolved precession experiment, Fig. 10. One can analyze the change of J_{ex} from the global macro-spin dynamics of the antiferromagnetic order parameter after a photo-doping excitation: The dynamics of the sub-lattice magnetization $\boldsymbol{M}_1$ on one of the two sub-lattices of the anti-ferromagnet is determined by the precession of the moment $\boldsymbol{M}_1$ in an effective magnetic field $\boldsymbol{B}_{\text{eff}} = J_{ex}\boldsymbol{M}_2 + \boldsymbol{B}$ given by the exchange coupling to the other sub-lattice and the external field,

$$\frac{d}{dt}\boldsymbol{M}_1 = (J_{ex}\boldsymbol{M}_2 + \boldsymbol{B}) \times \boldsymbol{M}_1, \text{ and } 1 \leftrightarrow 2. \tag{82}$$

In equilibrium, the static external field implies a canted anti-ferromagnetic state (Fig. 10). If the photo-doping modifies the effective parameter J_{ex}, spins are no longer aligned with $\boldsymbol{B}_{\text{eff}}$ and start to precess. From the precession dynamics, which can be obtained from the DMFT solution of the photo-excited Hubbard model, one can thus read off J_{ex}. As shown in Fig. 10, one finds an exchange interaction which is different from the equilibrium state of the half-filled model, but roughly equals the value obtained in an equilibrium state with the same density of carriers $n - 1 = 2n_{ex}$ [56].

Multi-orbital systems

The previous analysis shows that photo-doping provides an ultra-fast way to manipulate materials properties. The photo-doped state in the single-band anti-ferromagnet is controlled (after some primary electronic relaxation) by a single control parameter n_{ex}. This may be expected from the simplicity of the model, which has only a single band and is particle-hole symmetric,

such that hole-doping, electron doping, and photo-doping have a similar effect. In more complex models, in particular those involving more than one orbital, there is a large playground to manipulate the occupations of different types of doubly occupied and multiply occupied states [57] and use this to modify the effective interactions which govern spin and orbital order. A recent investigation of photo-doping in the two-orbital Hubbard model at quarter filling has revealed a possible path to reach hidden states by photo-doping [58]: For one electron in two degenerate orbitals of e_g symmetry, the Hubbard model features both spin and orbital order in equilibrium, analogous to the order in $KCuF_3$ [59]. Photo-excitation is followed by non-thermal melting, which results in a transient reduction of the two orders. In contrast to the effect of heating, however, the magnetic order melts consistently slower than the orbital order. The photo-doped state therefore has a intrinsically different spin-orbital order from the equilibrium state, and the coupling between the two order parameters leads to a ferro-orbital state, which can otherwise not be established in the equilibrium phase diagram.

5 Outlook and further questions

In these notes we have presented the theoretical basis for a description of correlated electron systems out of equilibrium using non-equilibrium DMFT. These lecture notes do not represent a review of non-equilibrium DMFT. For example, a large field of research which has been left out includes the so-called Floquet engineering of Hamiltonians by periodic driving [10], where DMFT provides a framework to study directly the driven dissipative state [13]. Rather than listing all this work, we end this lecture with a loose list of questions and topics which remain open for further research:

- **Multi-orbital effects**: Many correlated materials have more than one active orbital, so that their physics is governed by the interplay of orbital order, spin-order, and the strong coupling to the lattice. In such systems, intertwined order parameters allow to steer a system along nontrivial pathways into novel transient or hidden phases, or dynamically stabilize non-equilibrium states, such as already seen in Ref. [58]. Some interesting directions to be explored further, such as photo-induced metal-insulator transitions have already been demonstrated within the Gutzwiller approximation [60]. The investigation of multi-orbital effects within DMFT is clearly only at the beginning.

- **Long term steady states**: Non-equilibrium steady states have so far been used to investigate driven steady states (e.g., to discuss current-induced phase transitions [61]). An interesting open question is whether one can design an approximate non-equilibrium steady state description of pre-thermalized or photo-doped states in correlated systems.

- **Impurity solvers**: There are currently no non-perturbative impurity solvers which work at long times. While NCA can be applied very flexibly within the Mott phase, it becomes increasingly inaccurate for correlated metallic phases. An interesting perspective

is given by the application of the non-perturbative methods (QMC [37] and Hamiltonian-based solvers [39]), which currently seem to be too expensive for the long-term transient dynamics, to explore the non-equilibrium steady states.

- **Role of non-local correlations**: DMFT assumes a spatially local self-energy. One might wonder whether the local approximation, though correct in the limit of taking the coordination number Z to infinity at a fixed length of the time contour, would miss qualitatively important effects for finite-dimensional systems. Most likely, the long-time limit and the $Z \to \infty$ limit do not commute, i.e., even in highly coordinated systems at some timescale there may be effects which have a qualitative influence on the dynamics that is not captured by DMFT. This includes the influence of short-range fluctuations on the relaxation dynamics, such as discussed around Fig. 9, or the feedback of collective excitations on the non-equilibrium dynamics. These effects may be investigated to first approximation using diagrammatic approximations such as GW or FLEX.

- **Non-local interactions, screening, and the path towards an ab-initio description**: An important consequence of non-local interactions is the feedback of the long-range Coulomb interaction on the parameters of the model Hamiltonians via dynamical screening. For large excitation densities, or interactions involving many bands, one can expect a sizeable renormalization of the Hubbard U via screening, which may even close a Mott gap. A possible way to include these effects is via the extended DMFT formalism [62]. The question of screening is also closely related to the possible ab-initio determination of model parameters. Other than in equilibrium, an ab-initio formalism comparable to density functional theory is less developed. The combination of a non-equilibrium Green function approach such as DMFT with a density-functional approach suffers from the double counting problem, which is unresolved in equilibrium. An interesting perspective is therefore the combination of non-equilibrium GW with DMFT [63], which can be formulated in a consistent functional language. The main challenge in this direction is, again, the solution of the resulting impurity problem with retarded interactions which can currently only be solved in the limited parameter regime accessible by NCA.

Acknowledgements

References

[1] C. Giannetti, M. Capone, D. Fausti, M. Fabrizio, F. Parmigiani, and D. Mihailovic,
Adv. Phys. **65**, 58 (2016)

[2] T. Rohwer *et al.*, Nature **471**, 490 (2011)

[3] D. Fausti, R.I. Tobey, N. Dean, S. Kaiser, A. Dienst, M.C. Hoffmann, S. Pyon,
T. Takayama, H. Takagi, A. Cavalleri, Science **331**, 189 (2011)

[4] Mitrano *et al.*, Nature **530**, 461 (2016)

[5] S. Mor *et al.*, Phys. Rev. Lett. **119**, 086401 (2017)

[6] D. Wegkamp *et al.*, Phys. Rev. Lett. **113**, 216401 (2014)

[7] H. Ichikawa *et al.*, Nat. Mater. **10**, 101 (2011)

[8] L. Stojchevska, I. Vaskivskyi, T. Mertelj, P. Kusar, D. Svetin, S. Brazovskii, and
D. Mihailovic, Science **344**, 177 (2014)

[9] M. Först, C. Manzoni, S. Kaiser, Y. Tomioka, Y. Tokura, R. Merlin, and A. Cavalleri,
Nat. Phys. **7**, 854 (2011)

[10] M. Bukov, L. D'Alessio, and A. Polkovnikov, Adv. Phys. **64**, 139 (2015)

[11] T. Oka and H. Aoki, Phys. Rev. B **79**, 081406(R) (2009)

[12] M. Knap, M. Babadi, G. Refael, I. Martin, and E. Demler, Phys. Rev. B **94**, 214504 (2016)

[13] Y. Murakami, N. Tsuji, M. Eckstein, and Ph. Werner, Phys. Rev. B **96**, 045125 (2017)

[14] J.H. Mentink, K. Balzer, and M. Eckstein, Nat. Commun. **6**, 6708 (2015)

[15] F. Görg, M. Messer, K. Sandholzer, G. Jotzu, R. Desbuquois, and T. Esslinger,
Nature **553**, 481 (2018)

[16] O. Schubert *et al.* Nat. Photonics **8**, 119 (2014)

[17] A. Polkovnikov, K. Sengupta, A. Silva, and M. Vengalattore,
Rev. Mod. Phys. **83**, 863 (2011)

[18] M. Eckstein, M. Kollar, and Ph. Werner, Phys. Rev. Lett. **103**, 056403 (2009)

[19] M. Kollar, F.A. Wolf, and M. Eckstein, Phys. Rev. B **84**, 054304 (2011)

[20] A. Georges, G. Kotliar, W. Krauth, and M.J. Rozenberg, Rev. Mod. Phys. **68**, 13 (1996)

[21] E. Pavarini, E. Koch, D. Vollhardt, and A. Lichtenstein (eds.): *DMFT at 25:
Infinite Dimensions*, Modeling and Simulation Vol. 4 (Forschungszentrum Jülich, 2014)

[22] P. Schmidt, and H. Monien, arXiv:cond-mat/0202046.

[23] J.K. Freericks, V.M. Turkowski, and V. Zlatić, Phys. Rev. Lett. **97**, 266408 (2006)

[24] H. Aoki, N. Tsuji, M. Eckstein, M. Kollar, T. Oka, and Ph. Werner,
Rev. Mod. Phys. **86**, 779 (2014)

[25] A. Kamenev, *Field Theory of Non-Equilibrium Systems*
(Cambridge University Press, 2011)

[26] H. Haug, and A. Jauho, *Quantum Kinetics in Transport and Optics of Semiconductors*
(Springer, 2008)

[27] J.K. Freericks, H.R. Krishnamurthy, and Th. Pruschke,
Phys. Rev. Lett. **102**, 136401 (2009)

[28] M. Eckstein and M. Kollar, Phys. Rev. B **78**, 245113 (2008)

[29] F. Randi, D. Fausti, and M. Eckstein, Phys. Rev. B **95**, 115132 (2017)

[30] F. Randi, M. Esposito, F. Giusti, F. Parmigiani, O. Misochko, D. Fausti, and M. Eckstein,
arXiv:1705.08523 (to appear in Phys. Rev. Lett.)

[31] G. Baym and L.P. Kadanoff, Phys. Rev. **124**, 287 (1961)

[32] H. Brunner and P.J. van der Houwen, *The Numerical Solution of Volterra Equations*
(Elsevier, 1986)

[33] M. Eckstein, M. Kollar, and Ph. Werner, Phys. Rev. B **81**, 115131 (2010)

[34] M. Bonitz (edt.), *Progress in Nonequilibrium Green's Functions*
(World Scientific, Singapore, 2000)

[35] W. Metzner and D. Vollhardt, Phys. Rev. Lett. **62**, 324 (1989)

[36] E. Gull, A.J. Millis, A. Lichtenstein, A.N. Rubtsov, M. Troyer, and Ph. Werner,
Rev. Mod. Phys. **83**, 349 (2011)

[37] G. Cohen, E. Gull, D.R. Reichman, and A.J. Millis, Phys. Rev. Lett. **115**, 266802 (2015)

[38] F.A. Wolf, I.P. McCulloch, and U. Schollwöck, Phys. Rev. B **90**, 235131 (2014)

[39] Ch. Gramsch, K. Balzer, M. Eckstein, and M. Kollar, Phys. Rev. B **88**, 235106 (2013)

[40] E. Arrigoni, M. Knap, and W. von der Linden, Phys. Rev. Lett. **110**, 086403 (2013)

[41] M. Eckstein and Ph. Werner, Phys. Rev. B **82**, 115115 (2010)

[42] M. Eckstein and Ph. Werner, Phys. Rev. B **84**, 035122 (2011)

[43] N. Strohmaier, D. Greif, R. Jördens, L. Tarruell, H. Moritz, T. Esslinger, R. Sensarma, D. Pekker, E. Altman, and E. Demler, Phys. Rev. Lett. **104**, 080401 (2010)

[44] Z. Lenarčič and Peter Prelovšek, Phys. Rev. B **90**, 235136 (2014)

[45] H. Okamoto, T. Miyagoe, K. Kobayashi, H. Uemura, H. Nishioka, H. Matsuzaki, A. Sawa, and Y. Tokura, Phys. Rev. B **82**, 060513(R) (2010)

[46] M. Mitrano *et al.*, Phys. Rev. Lett. **112**, 117801 (2014)

[47] Z. Lenarčič, M. Eckstein, and Peter Prelovšek, Phys. Rev. B **92**, 201104(R) (2015)

[48] L. Perfetti, P.A. Loukakos, M. Lisowski, U. Bovensiepen, H. Berger, S. Biermann, P.S. Cornaglia, A. Georges, and M. Wolf, Phys. Rev. Lett. **97**, 067402 (2006)

[49] M. Ligges *et al.*, Phys. Rev. Lett. **120**, 166401 (2018)

[50] Ph. Werner, K. Held and M. Eckstein, Phys. Rev. B **90**, 235102 (2014)

[51] M. Wais, M. Eckstein, R. Fischer, P. Werner, M. Battiato, and K. Held, arXiv:1806.02570.

[52] Ph. Werner, N. Tsuji, and M. Eckstein, Phys. Rev. B **86**, 205101 (2012)

[53] N. Tsuji, M. Eckstein, and Ph. Werner, Phys. Rev. Lett. **110**, 136404 (2013)

[54] S. Dal Conte *et al.*, L. Vidmar, *at al.*, Nat. Phys. **11**, 421 (2015)

[55] M. Eckstein and Ph. Werner, Sci. Rep. **6**, 21235 (2016)

[56] J.H. Mentink and M. Eckstein, Phys. Rev. Lett. **113**, 057201 (2014)

[57] H.U.R. Strand, D. Golež, M. Eckstein, and Ph. Werner, Phys. Rev. B **96**, 165104 (2017)

[58] J. Li, H.U.R. Strand, P. Werner, and M. Eckstein, arXiv:1806.01567.

[59] E. Pavarini, E. Koch, and A.I. Lichtenstein, Phys. Rev. Lett. **101**, 266405 (2008)

[60] M. Sandri and M. Fabrizio, Phys. Rev. B **91**, 115102 (2015)

[61] A. Matthies, J. Li, and M. Eckstein, arXiv1804.09608.

[62] D. Golez, M. Eckstein, and Ph. Werner, Phys. Rev. B **92**, 195123 (2015)

[63] D. Golez, L. Boehnke, H. Strand, M. Eckstein, and Philipp Werner, Phys. Rev. Lett. **118**, 246402 (2017)